Energy Calibration of Neutrino Telescopes Using Ultra High Energy Tau Neutrinos

Licentiate Thesis
by Pär Lindahl

Stockholm University, Department of Physics
and
Kalmar University, Department of Technology
2003

Licentiate Dissertation 2003
Fysikum
Stockholm University
Roslagstullsbacken 21
SE – 106 91 Stockholm

Abstract

High-energy neutrinos have the potential of conveying information from the edge of the universe and from deep inside the most cataclysmic high-energy processes. To detect these weakly interacting particles very large neutrino telescopes like AMANDA – which is deployed in the South Pole ice cap – are needed to reach substantial detection rates. The detection principle used in AMANDA and its planned extension – the 1 km^3 detector IceCube – is to register the Čerenkov photons emitted by charged particles propagating through the transparent detector medium (ice). Charged particles are produced as a result of neutrino-nucleon reactions, and the photon production is related to the energy of the parent neutrino. This makes energy reconstruction possible.

In this thesis a calibration method is suggested for neutrinos above ~1 PeV, where the flux of cosmic tau neutrinos would be used as a natural calibration "beam". The most likely interaction scheme for tau neutrinos, the "double bang" signature, consists of two particle cascades separated by a relativistic tauon. The first cascade is a result of the charged current interaction with a nucleon, and the second cascade is a result of the tauon decay. Due to the relativistic time dilation of the tauon lifetime the tauon range is proportional to its energy. Thus, the observed cascade separation could provide an independent measure of the observed energy for the second cascade of the signature. This is the basis of the proposed calibration method.

After a brief review of a few proposed neutrino sources, the AMANDA and IceCube detectors are described, resulting in a simple parameterized "effective volume" expression. For both detectors the free parameters of this expression are determined through Monte Carlo simulations reaching excellent agreement between the two representations. The expected double bang detection rates for different sources are then estimated. E.g. following an example by *Alvarez-Muñiz*/*Halzen*/*Hooper* (2002), determining the maximal detection rate in a generic 1 km^3 detector due to down going neutrinos from GRBs (one of the possible sources), an improved value – 0.15 double bang events per year – is found. This is about four times smaller than the earlier result.

Finally, the calibration procedure is demonstrated, showing that the proposed method may be applicable for IceCube sized detectors given a tau neutrino flux approaching the upper limit inferred from AMANDA-B10 data.

In addition, this thesis also contains a presentation of experimental work performed both in the laboratory (timing properties in a detector channel and ice freezing experiments) and at the AMANDA facility at the South Pole (an all-channel survey over some characteristic properties in the AMANDA-B13 detector). Also presented is a Monte Carlo code developed for detailed simulation of detector properties, and a simple expression derived for estimating the background trigger rate due to so-called "dark noise" in a photo multiplier tube (PMT).

To Pia and David with love!

Contents

Chapter 1

Introduction

High-energy neutrinos have the potential to convey information from the edge of the universe and from deep inside the most cataclysmic high-energy processes. These particles may also reveal the presence of the elusive “dark matter”, which is suspected to contribute the dominating portion of the mass density on cosmic scales. By recent development of the first generation of high-energy neutrino telescopes a new promising “window” has been opened toward the universe.

The largest existing and future neutrino telescopes are designed to detect the Čerenkov photons emitted by charged particles produced as a result of neutrino-nucleon reactions. The detector medium for these detectors is naturally occurring water (BAIKAL [1], ANTARES [2], NESTOR [3] and NEMO [4]) or ice (AMANDA [5] and IceCube [6]).

Several features of the interacting neutrino may be derived from the detection of Čerenkov photons propagating through the detector volume. These features include direction-of-origin and energy of the neutrino. However, since this is an indirect measurement — the detected particles are the daughters of a neutrino-nucleon interaction — it is appropriate to separate the analysis of an event into two parts: First the relevant properties of the charged particles are determined. Then these results are used to derive information about the parent neutrino.

To be able to perform the first step one needs to calibrate the detector. This involves detailed *investigations* determining the properties of the different subsystems and how they interact with each other. The second step, which is an interpretation of the measurement, depends on knowledge about the neutrino-nucleon interaction and on the expected neutrino flux.

In this thesis I propose a method for energy calibration of neutrino telescopes. In contrast to accelerator based experiments, in which a detector may be calibrated by exposing it to a beam with known composition and energy and then measure its response, the calibration of the neutrino telescopes discussed here is more dependent on detailed *simulations* of every part of the detection process. This includes particle reactions in the material inside and surrounding the detector, photon propagation through the detector medium, photon detection and the response of the accompanying electronics.

To determine the validity of the simulation results it would of course be advantageous if one could identify a subset of reactions in the detector where the energy deposit can be determined by some independent method. This subset could then be used for calibration in a similar fashion as with a man-made calibration beam. In this thesis I investigate the possibility to use one such subset, described by the so-called ”double bang signature” [7], two particle cascades separated by the flight of a relativistic tauon. The first cascade and the appearance of the tauon is the result of a charged current (CC) tau neutrino reaction with a nucleon. The second cascade is the result of the tauon decay. Since the tauon decays in flight its mean range is proportional to its energy — a fact useful for calibration purposes.

In the proposed calibration scheme one uses reconstructed cascade separations for a set of double bang events to estimate the corresponding second-cascade energy deposits. For each event one also reconstructs the energy deposit using the default algorithm for the detector. An important cross-check for this algorithm may then be obtained by comparing the two sets of energy estimations.

To be able to evaluate the prospects for this calibration method one needs to address three questions:

1) Are tau neutrinos of sufficient energy (~1 PeV) produced in nature?
   - An outline of the theoretical and experimental indications is presented in chapter 2.
2) If tau neutrinos *are* produced in nature, under what conditions will the present or planned neutrino telescopes be able to detect them?
   - In chapters 3 and 4 the AMANDA and IceCube detectors are presented, including a description of a work regarding the properties of the detector electronics in AMANDA.
   - In chapters 5, 6, 8 and 9 the double bang signature and its detection are described in some detail.
3) If tau neutrinos *are* detected, under what conditions can the double bang signature be used for calibration purposes?
   - In chapter 10 I present an investigation of the calibration method using simulated double bang events.
   - In chapter 7 I present all simulation tools used for generation of tau neutrinos, simulation of the detector response and for the subsequent analysis of the double bang events.

The final chapter of this thesis, chapter 11, contains a summary and an outlook towards future investigations.

Chapter 2

High-energy neutrinos

2.1 Scientific motivation for neutrino astronomy

With the advent of neutrino telescopes sensitive in the highest energy range, a new window is opened to the universe. Several questions in particle physics and astrophysics may be addressed through observations that are complementary (and supportive) to other detection methods.

Many proposed sources of high-energy neutrinos will also emit gamma rays and various charged particles. If the *charged* particles encounter any electric or magnetic fields as they propagate through space they will be deflected, thus potentially loosing the information about their direction of origin. The electrically *neutral* gamma rays and neutrinos, on the other hand, will travel in straight lines (i.e. along geodesics). However, with increasing energy, the cross-section increases for gamma rays to interact, predominantly through pair production with the low-energy photons constituting the *cosmic microwave background radiation* (CMBR). This attenuation limits the accessible range for gamma-ray telescopy, and also modifies the gamma-ray spectrum. Neutrinos do not suffer from these limitations, since they only interact through the weak force (and gravity). This fact also allows neutrinos to escape from dense regions that are obscured for other types of radiation.

Through high-energy neutrino astronomy it may be possible to investigate the nature of the dark matter, to search for the origin of the cosmic rays, to probe the physical processes responsible for the energy release in the most luminous objects in the universe, and to study the phenomenon of neutrino oscillation between flavors. In addition, there is also the very real possibility to unveil something completely unexpected, as has happened before when new observation methods has been introduced.

In this chapter a few potential sources for high-energy neutrinos are presented, followed by introductions to some effects of neutrino oscillation and neutrino interaction with matter. Finally, the expected neutrino flux is indicated through a few examples on theoretical flux estimations and experimental upper limits.

2.2 Neutrino sources

2.2.1 Dark matter annihilation

Studies of the anisotropy of the CMBR [8] and of the magnitude-redshift distribution for *Ia*-type super-novae [9] suggest that dark matter constitute close to 83% of the matter in the universe [10]. Dark matter only manifests itself through its gravitational influence on its surroundings. Its nature is not known, but candidates are generically labeled "hot" for relativistic constituents or "cold" for non-relativistic ones.

One group of particles among the cold-dark-matter candidates is the *weakly interacting massive particles* (WIMPs), whose existence is proposed by some supersymmetric theories. These particles may have been gravitationally trapped inside massive astronomical bodies, like the Sun or the Earth, leading to increased annihilation rates at these sites [11]. The particles produced in the annihilation process will decay. Among the decay products there will be neutrinos, with a broad energy spectrum bounded from above by the WIMP mass. Cosmological arguments suggest that such cold dark matter candidates should have a mass below ~10 TeV [11].

The search for a neutrino signal from the Sun or the Earth at energies compatible with the WIMP models will contribute both to fundamental particle physics and to cosmology.

2.2.2 Cosmic-ray interactions

The cosmic rays mainly consist of light nuclei, with a very broad energy range. The flux of these particles has been measured over many decades in energy, and the differential energy spectrum can be described by a segmented power-law formula [12]

$$\frac{\mathrm{d}N_{\mathrm{CR}}}{\mathrm{d}E_{\mathrm{CR}}} \propto E_{\mathrm{CR}}^{-\alpha} \tag{2.1}$$

with the following values for the spectral index:

$$\alpha = \begin{cases} 2.7 & E < 10^{16}\,\mathrm{eV} \\ 3.0 & 10^{16} < E < 10^{18}\,\mathrm{eV} \end{cases} \tag{2.2}$$

Above 10^{18} eV the spectral index appears to be somewhat smaller. (Observations extend to energies above 10^{20} eV.)

The origin of the cosmic rays is not known, mainly due to the fact that the interstellar magnetic field within our galaxy deflects these charged particles. It is therefore difficult to associate them with any particular point (object) in the sky. It is, however, known that the sources for the most energetic cosmic-ray particles cannot be arbitrarily distant. This is due to attenuation: Regardless of its nature, cosmic-ray particles above 10^{19} eV will interact, predominantly with the CMBR, making the universe opaque at distances larger than ~100 Mpc [13]. Due to the energy dependence of the attenuation, the observed cosmic-ray spectrum is steeper than the emitted spectrum.

From the cosmic-ray sources also neutrinos will emerge, and this flux will be less affected by the interstellar and intergalactic media: There will be less attenuation, allowing neutrinos to reach us from the entire observable universe. Also, the neutrino spectrum will suffer less distortion (and will thus be more "flat") than the cosmic-ray spectrum.

In addition to the direct neutrino emission from the cosmic-ray sources, the cosmic rays will produce neutrinos as a result of interactions with various matter- and radiation targets. *Matter targets* include the interstellar matter in the galactic disk, the Sun and the Earth's atmosphere. An important *radiation target* is the CMBR. Since the most common cosmic-ray particle is the proton, the neutrino production may be exemplified by considering the result from $p + p$ or $p + \gamma$ interactions. In these processes large amounts of pions will be produced. The neutral pion will decay into two photons, and the charged pions will follow the decay chain[*]: $\pi \rightarrow \mu + \nu_\mu$ followed by $\mu \rightarrow \nu_\mu + e + \nu_e$. This scenario suggests that muon neutrinos are twise as abundant as electron neutrinos [14]. For a "thin" target the majority of the pions will decay (and produce neutrinos) instead of further interacting with the target material. The neutrino spectrum for such a target will thus follow the shape of the cosmic-ray spectrum. For "dense" targets, interactions with the target will compete with decay, especially at higher energies, thus producing a steeper neutrino spectrum.

Some of the neutrino-flux components from cosmic-ray interactions with known targets can be calculated, and may serve as reference fluxes. The hope is to be able to identify some high-energy neutrino point sources above this "background", indicating the possible cosmic-ray sources. But even if these sources would turn out to be too weak neutrino emitters to be individually identified, the calorimetric information from their collective flux would (if it could be measured) provide important information about the nature of these sources.

2.2.3 Gamma-ray bursters

A flux of high-energy hadrons (possible primaries for high-energy neutrino production) may be produced through either direct acceleration of such particles ("bottom-up" production) or through hadronic decay of extremely massive particles ("top-down" production). A number of phenomena involving acceleration are known today. The most luminous of these is the *gamma-ray burst* (GRB), which are events (of extragalactic origin) lasting between a few tens of milliseconds to a few hundred seconds [12].

One plausible model for the GRBs is the "relativistic fireball model" by Meszárós & Rees (see e.g. [15]) in which gravitational energy is released through the collapse of a massive star or the merging of two star remnants (neutron stars and/or black holes). The collapse/merging is followed by an ultra-relativistic expansion. Accelerated electrons will produce gamma rays through synchrotron radiation, and as the plasma becomes transparent the gamma rays are released. Also protons will be accelerated, and pions will be produced in the following $p + \gamma$ interactions. In turn, the pions will decay and thus produce neutrinos.

[*] No distinction has been made between a particle and its antiparticle.

The theoretical framework for describing acceleration of particles associated with supersonic shocks in a plasma is called "Fermi acceleration" [16]. The differential energy spectrum for the accelerated charged particles, and thus of the produced gamma rays and neutrinos, can be described by a power-law formula. The typical value for the spectral index is $\alpha = 2$. Thus, for neutrinos

$$\frac{\mathrm{d}N_\nu}{\mathrm{d}E_\nu} \propto E_\nu^{-2} \ . \tag{2.3}$$

2.2.4 Active galactic nuclei

Roughly 1% of all galaxies possess an active nucleus, from which more power is emitted than e.g. the collective radiation from all the stars in our galaxy. It is believed that these *active galactic nuclei* (AGN) are powered by super-massive black holes, causing acceleration and accretion of surrounding material [15]. In these processes strong shocks are formed, leading to Fermi acceleration of charged particles.

If protons are among the accelerated particles they will produce pions through $p + p \rightarrow \cdots \rightarrow \pi^{\pm} + \text{"}anything\text{"}$ or $p + \gamma \rightarrow \Delta^{+} \rightarrow n + \pi^{+}$ interactions, and neutrinos will emerge as the pions decay.

2.2.5 Topological defects

Both GRB:s and AGN:s could produce the most energetic cosmic-ray particles through acceleration of charged particles (bottom-up production). An alternative mechanism to produce these cosmic-ray particles is through hadronic decay of extremely massive (GUT scale: ~10^{24} eV) particles (top-down production). Such massive particles may be produced by radiation, interaction or collapse of "topological defects" like monopoles, cosmic strings, etc [13] [17].

2.3 Neutrino oscillation

Neutrinos produced in $p + p$ or $p + \gamma$ interactions are not evenly distributed between the three neutrino flavors. According to what has been pointed out in section 2.2.2 muon neutrinos and electron neutrinos are the products of charged-pion decays, with twice as many muon neutrinos as electron neutrinos. The main source for "prompt" tau neutrinos is the decay of charged $D_S^{\pm}$ mesons [14]. However, the cross-section for $D_S^{\pm}$ production is ~4 orders of magnitude smaller than that of charged-pion production. In addition tau neutrinos are only produced in ~3% of the $D_S^{\pm}$ decays [18]. Thus, the expected flavor mix from these sites is (roughly) 1:2:<10^{-5} for electron neutrinos, muon neutrinos and tau neutrinos respectively.

Even if only a very small fraction of the neutrinos produced in the universe are tau neutrinos – due to so-called called "neutrino mixing" – all three neutrino flavors will be equally abundant since neutrinos are oscillating between flavors as they propagate., This was first shown by the Super-Kamiokande collaboration [19], and a consequence of their result is that half of the generated muon neutrinos within any sufficiently large energy interval will have converted into tau neutrinos before reaching Earth:

The probability for a muon neutrino (ν_μ) of energy E_ν to be converted into a tau neutrino (ν_τ) at a distance x from the source is given by

$$P(\nu_\mu \to \nu_\tau) = \sin^2(2\theta)\sin^2\left[\frac{x}{L_\nu(E_\nu)}\pi\right] \tag{2.4}$$

(see for example [12]) where θ is the mixing angle, and the oscillation length for the mass-difference squared $\Delta m^2 = \left|m_{\nu_\tau}^2 - m_{\nu_\mu}^2\right|$ is

$$L_\nu(E_\nu) = \frac{2E_\nu h}{\Delta m^2 c^3} = 2.48\cdot 10^3\left(\frac{E_\nu}{1\text{GeV}}\right)\left(\frac{1\text{eV}^2/c^4}{\Delta m^2}\right) \text{ meters.} \tag{2.5}$$

Results from the Super-Kamiokande experiment indicate that oscillation between muon neutrinos and tau neutrinos takes place with near maximal mixing, $\sin^2(2\theta) = 1$, with a favored mass-difference squared of $\Delta m^2 = 3.2\cdot 10^{-3}$ (eV^2/c^4) [19]. The corresponding oscillation length according to equation (2.5) is

$$L_\nu(E_\nu) = 7.8\cdot 10^5\left(\frac{E_\nu}{1\text{GeV}}\right) \text{ meters } = 8.2\cdot 10^{-5}\left(\frac{E_\nu}{1\text{PeV}}\right) \text{ light-years.} \tag{2.6}$$

For a source at a fixed distance $x >> L_\nu(E_\nu)$ the conversion probability according to equation (2.4) is a rapidly oscillating function with energy. By inserting equation (2.6) into (2.4) the energy separation between two minima can be approximated by a continuous function:

$$\Delta E(E_\nu) \approx 8.2\cdot 10^{-5}\left(\frac{1\text{ly}}{x}\right)\left(\frac{E_\nu}{1\text{PeV}}\right)^2 \text{ PeV,} \tag{2.7}$$

where E_ν is in the interval between the two minima.

If ΔE is much smaller than the energy resolution (σ_E) of the detector, the conversion probability averaged over some appropriate energy interval (centered at E_ν) may be used as an *effective* conversion probability. Assuming a slowly varying energy spectrum this effective conversion probability is given by

$$P_{\text{eff}}(E_\nu) = < P(E_\nu) > = \tfrac{1}{2\sigma_E}\int_{E_\nu-\sigma_E}^{E_\nu+\sigma_E} P(\nu_\mu \to \nu_\tau)\mathrm{d}E_\nu \approx$$

$$\approx \tfrac{1}{2}\sin^2(2\theta) \quad ; \qquad x >> L_\nu(E_\nu)\,,\ \sigma_E >> \Delta E\ , \tag{2.8}$$

i.e. a constant, only depending on the mixing angle.

This thesis focuses on the possible detection of tau neutrinos, with their energies in the interval $1\,\text{PeV} < E_\nu < 100\,\text{PeV}$, through the so-called "double bang" signature (presented in section 6.1). According to equation (2.6) the oscillation length $L_\nu(100\,\text{PeV}) \approx 10^{-2}$ ly, which is much less than the distance to the closest star, α *Centauri*, at 4.3 ly. For a neutrino source at $x \approx 4$ ly the energy separation between probability minima according to equation (2.7) is $\Delta E(100 PeV) \approx 0.2$ PeV, which is much smaller than the achievable energy resolution at these neutrino energies (see section 5.2.4). Thus, at *ultra-high energies* (UHE) the requirements of equation (2.8) are fulfilled for any neutrino sources "outside" the solar system (i.e. at distances greater than that of the closest stars).

Resent results [20] and [21] show that electron neutrinos also participate in the oscillation scenario. All three neutrino flavors are thus involved in this phenomenon. In the estimations of the expected tau neutrino detection rates presented in chapter 9 it is assumed that, due to oscillation between neutrino flavors, one third of all UHE neutrinos (from distant sources) are tau neutrinos.

2.4 Neutrino interactions

2.4.1 Neutrino + nucleon cross-sections

Neutrinos interact with quarks and leptons through the weak force, which is mediated by either an electrically charged particle, the $W^{\pm}$, (*charged current* (CC) interaction) or a neutral particle, the Z^0, (*neutral current* (NC) interaction). The cross-section for these reactions is very small. This allows neutrinos to travel over cosmological distances without scattering. On the other hand, the low interaction probability imposes a need for very large detectors, to be able to reach a reasonably high detection rate.

As neutrinos encounter a matter target reactions will take place with both electrons and nucleons. However, for neutrinos with energies in the range $1\,\text{PeV} \le E_\nu \le 100\,\text{PeV}$ the cross-section for $\nu + e$ reactions is very small compared with the cross-section for $\nu + nucleon$ reactions[*]. Therefore, only reactions with nucleons will be considered here.

With the nucleons at rest, the cross-section increases monotonically with neutrino energy as smaller details of the internal structure of the nucleon become "visible" to the neutrino. At low energies the cross-section may be measured experimentally, but to estimate the cross-section at higher energies one is forced to make extrapolations. One modern set of CC and NC cross-section estimates is presented in [22]. These cross-sections are shown in figure 2.1 for a broad energy range. It may be noted that no distinction has been made between the three neutrino flavors, since their cross-sections are all expected to be very similar at these energies. Furthermore, the cross-sections for neutrino- and *anti*neutrino reactions are similar, and the difference will be neglected here.

[*] The only exception is the "resonance" at 6.3 PeV for $\overline{\nu_e} + e$ reactions.

Also shown in figure 2.1 is a suggested parameterization for the total cross section (σ_{tot}). This parameterization was obtained by minimizing the relative error compared with the estimates in [22] over the presented energy interval:

$$\sigma_{\text{tot}}(E_\nu) = \sigma_1 \left(\frac{E_\nu}{1\text{PeV}} \right)^{0.49} \quad ; \quad \sigma_1 = 8 \cdot 10^{-38} \text{ m}^2 \tag{2.9}$$

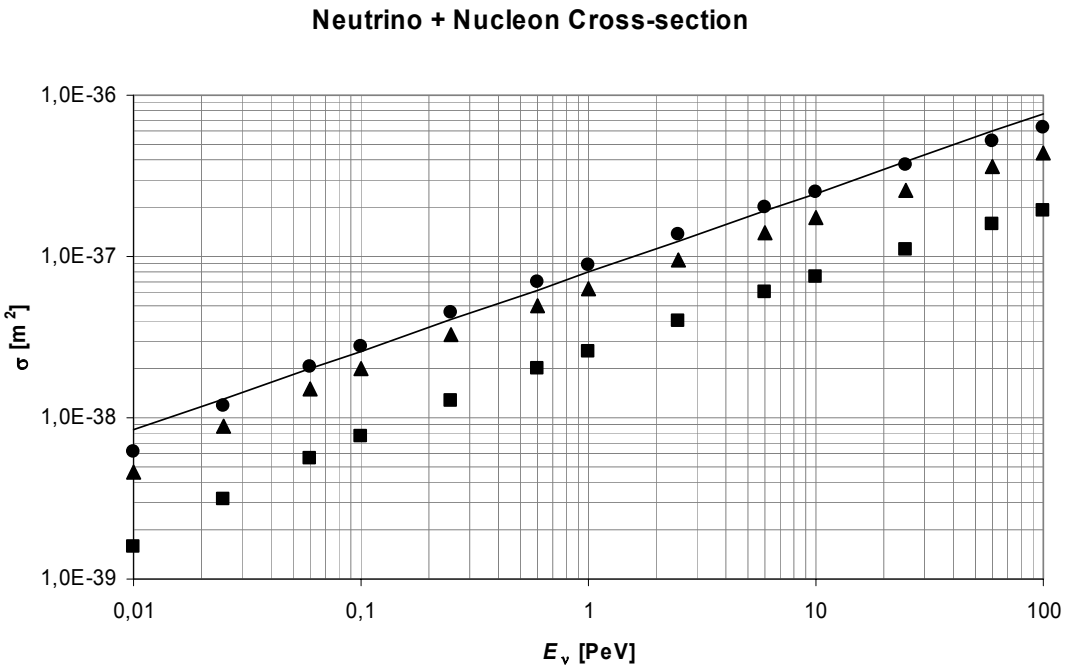

Figure 2.1 *ν + nucleon* cross-section estimates, calculated using the CTEQ4-DIS parton distributions [22]. Squares indicate NC cross-sections, triangles CC cross-sections and circles total (NC+CC) cross-sections. Also included in this plot is a suggested parameterization for the total cross-section: $\sigma_{\text{tot}}(E_\nu) = 8 \cdot 10^{-38} (E_\nu/1\text{PeV})^{0.49}$ m^2.

2.4.2 Earth shielding at high energies

One notable effect of the increasing cross-section with energy is that above some energy the Earth can no longer be regarded as transparent to neutrinos. This effect results in a reduced neutrino flux from "below" at high energies.

In [24] one defines by the *transparency energy* (E_{tr}) — the energy where the neutrino range is equal to the distance through the Earth along the trajectory towards the detector. This distance varies with nadir angle (θ), and so does the transparency energy. Under the approximations that the Earth may be regarded as a homogenous sphere with radius $R_{\oplus} \approx 6.4 \cdot 10^{6}$ m and density $\rho_{\oplus} \approx 5.5 \cdot 10^{3}$ kg/m^3, and using the parameterization of the total cross-section according to equation (2.9), the transparency energy is expressed by

$$E_{\mathrm{tr}} = \left(\frac{1}{2R_{\oplus} \cdot \cos\theta \cdot \sigma_1 \cdot \rho_{\oplus} \cdot N_{\mathrm{A}}} \right)^{1/0.49} \quad \text{PeV}, \tag{2.10}$$

where $N_{\mathrm{A}} \approx 6.0 \cdot 10^{26}$ kg^{-1} is the Avogadro constant.

As a neutrino interacts inside our planet it will loose some of its energy (or all, if no neutrino is among the daughters of the reaction). In NC reactions the neutrino will scatter (inelastically) against the nucleon in the same way for all types of neutrinos. In CC reactions (which are roughly twice as likely) the neutrino is converted into the corresponding charged lepton, with different results for the three flavors:

For an initial electron neutino an electron is created, which is rapidly brought to rest in matter. The electron is stable, and there will be no "secondary" neutrinos.

For an initial muon neutrino a muon is created. This lepton subsequently decays, producing a muon neutrino, an electron and an electron neutrino. However, before decaying the muon will propagate through matter. As its range in matter is much smaller than its decay length, it will loose most of its energy (through electromagnetic interactions) before decaying. The energy of the "secondary" neutrinos will therefore be well below the energy threshold of any high-energy neutrino telescope.

For an initial tau neutrino a tauon is created. This lepton decays through one of a large number of possible decay modes. There will however always be a tau neutrino present among the decay products. The lifetime of the tauon is much smaller than that of a muon (the decay may be regarded as essentially "prompt"), and the "secondary" neutrino(s) will be left with a substantial fraction of the initial energy. The Earth is therefore not entirely opaque to tau neutrinos above the transparency energy, but the energy of such neutrinos will be reduced. According to [24] the result will be a peak in the tau neutrino energy spectrum around the transparency energy. This peak characteristically follows a lognormal distribution, with a log scale r.m.s. width corresponding to approximately one decade in energy.

To make a rough estimate regarding the *detectable* tau neutrino flux from below one has to compare the transparency energy with the energy threshold of the detector. According to equation (2.10) the transparency energy at $\theta = 0°$ is ~0.08 PeV. For a detector with its threshold well above this energy, say at E_{th} = 1 PeV, the "peak" in the spectrum will not enter the sensitive region. As a "first order approximation" (for such a detector) one may therefore regard the Earth as *effectively* opaque to tau neutrinos from "below". In other words: 50% of the tau neutrino sky is shielded off by the Earth.

One approach to find a "second order approximation" (also including angular effects) is to assume that the Earth is opaque to tau neutrinos at nadir angles smaller than a certain boundary value, and transparent for larger values. Given this boundary angle (θ^{boundary}) it is then straightforward to calculate how much of the sky that would be shielded off by the Earth:

$$\frac{\varpi}{4\pi \text{ sr}} = \frac{1-\cos\theta^{\text{boundary}}}{2} \quad , \tag{2.11}$$

where ϖ is the solid angle shielded off by the Earth.

For small nadir angles the peak in the energy spectrum is below the threshold of the detector, and the Earth is *effectively* opaque to tau neutrinos. For sufficiently large angles the peak will be positioned within (or above) the energy interval where the detector is sensitive, and the Earth may be regarded as transparent. In the present context it seems reasonable to select a boundary angle for which the corresponding transparency energy ($E_{\text{tr}}^{\text{boundary}}$) is similar to the threshold of the detector. Using equation (2.10) the "shielding fraction" (the fraction of the sky shielded off by the Earth) may now be given as a function of this energy:

$$\frac{\varpi}{4\pi \text{ sr}} = \frac{1}{2}\left(1 - \frac{\left(E_{\text{tr}}^{\text{boundary}}\right)^{-0.49}}{2R_{\oplus}\cdot\sigma_1\cdot\rho_{\oplus}\cdot N_{\text{A}}}\right) \tag{2.11'}$$

In figure 2.2 the shielding fraction according to equation (2.11') is presented. From this plot it is apparent that, assuming $E_{\text{th}} \approx 1\,\text{PeV} \Rightarrow E_{\text{tr}}^{\text{boundary}} \approx 1\,\text{PeV}$, ~35% of the sky is shielded off by the Earth. Thus, the first- and second order approximations yield similar results.

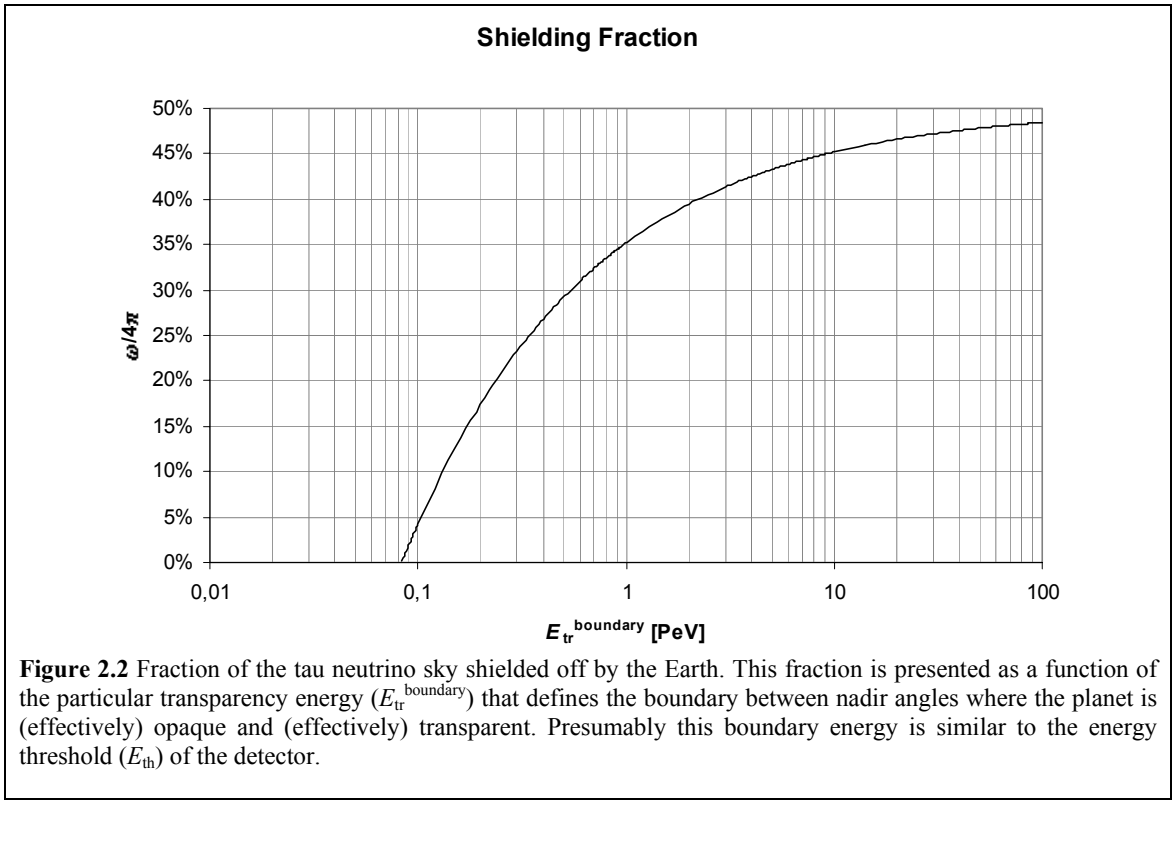

Figure 2.2 Fraction of the tau neutrino sky shielded off by the Earth. This fraction is presented as a function of the particular transparency energy ($E_{\text{tr}}^{\text{boundary}}$) that defines the boundary between nadir angles where the planet is (effectively) opaque and (effectively) transparent. Presumably this boundary energy is similar to the energy threshold (E_{th}) of the detector.

2.5 Flux estimations

In section 2.2 a number of potential sources of high-energy neutrinos are presented. Once identified, the next step is to try to estimate the neutrino fluxes from these sources. This may be done in several ways. For *individual source candidates* a direct approach may be adopted, where the flux estimates are based on models of the processes that lead to escaping neutrinos. Here are a couple of examples:

An attempt to calculate the muon neutrino flux from GRBs is presented in [25]. The flux is estimated for different values of the Lorentz boost factor (Γ) describing the bulk motion of the expanding fireball. This factor may vary between bursts. The maximal flux (extracted from figure 1 in [25]) is obtained for $\Gamma = 100$:

$$\Phi_{\nu_\mu+\bar{\nu}_\mu}^{\Gamma=100} \approx 2.5\cdot 10^{-3}\left(\frac{E_\nu}{1\text{PeV}}\right)^{-2} \ \text{PeV}^{-1}\cdot\text{m}^{-2}\cdot\text{yr}^{-1}\cdot\text{sr}^{-1} \quad ;$$

$$0.1\ \text{PeV} \le E_\nu \le 10^4\ \text{PeV} \qquad (2.12)$$

This upper limit is a time average value, assuming 1000 such GRBs/year. Note however, that the neutrinos are expected to coincide in time (within a few seconds, depending on neutrino mass) and direction with the gamma-ray counterparts. Furthermore, since GRBs are extragalactic events half of the muon neutrinos will have converted into tau neutrinos as they reach Earth, assuming that the two-flavor mixing scenario described in section 2.3 is applicable.

An attempt to calculate the muon neutrino flux from the cores of AGNs is presented in [26]. The flux for the collective neutrino emission from AGNs in the entire observable universe was extracted from figure 2 in [26]

$$\Phi_{\nu_\mu+\bar{\nu}_\mu} \approx 0.9\left(\frac{E_\nu}{1\ \text{PeV}}\right)^{-2} \ \text{PeV}^{-1}\cdot\text{m}^{-2}\cdot\text{yr}^{-1}\cdot\text{sr}^{-1} \quad ;$$

$$0.5\ \text{PeV} \le E_\nu \le 15\ \text{PeV} \qquad (2.13)$$

This flux is “diffuse” (i.e. it may be impossible to locate the source galaxy) and isotropic. Again, since these are extragalactic sources, half of the generated muon neutrinos will convert into tau neutrinos, assuming that the two-flavor mixing scenario described in section 2.3 is applicable.

For *classes of candidates* an indirect approach may be adopted where observations of e.g. the flux of the high-energy cosmic rays are used to put limits on the neutrino flux. This approach was used to obtain the so-called “Waxman-Bahcall upper bound” [27], which constrains the total neutrino flux from optically “thin” production sites, like e.g. GRBs and visible AGN jets:

$$\Phi_{\nu_\mu+\bar{\nu}_\mu}^{\text{WB}} \approx 5\cdot 10^{-3}\left(\frac{E_\nu}{1\ \text{PeV}}\right)^{-2} \ \text{PeV}^{-1}\cdot\text{m}^{-2}\cdot\text{yr}^{-1}\cdot\text{sr}^{-1} \qquad (2.14)$$

Note that this bound does not exclude the higher flux from AGN cores according to (2.13), since these production sites are not optically “thin”.

The *total flux of high energy neutrinos*, finally, is most readily constrained by direct neutrino observations. This has e.g. been done using data taken with the AMANDA-B10 detector during the austral winter from April to November 1997 [28]. The 90% confidence level upper limit is

$$\Phi_{\nu_\mu+\bar{\nu}_\mu} \approx 0.3\left(\frac{E_\nu}{1\,\mathrm{PeV}}\right)^{-2} \ \mathrm{PeV}^{-1}\cdot\mathrm{m}^{-2}\cdot\mathrm{yr}^{-1}\cdot\mathrm{sr}^{-1}\ ; \qquad 0.006\,\mathrm{PeV} \le E_\nu \le 1\,\mathrm{PeV} \qquad (2.15)$$

Note that this is a limit on the *observed* flux of muon neutrinos. If the two-flavor mixing scenario described in section 2.3 is applicable the *generated* flux is twice as large (where the missing fraction has been converted into tau neutrinos). Thus, the upper limit for the observed flux according to (2.15) is similar to what is expected from AGN cores according to (2.13).

Chapter 3

Neutrino telescopy with the AMANDA and IceCube detectors

3.1 Principle of detection

"AMANDA-II" is the largest existing neutrino telescope today (2003). It consists of 677 photo sensors (optical modules/OMs) deployed on 19 vertical strings to instrument a cylindrical volume – 500 m high and 200 m in diameter – at depths between 1500 m and 2000 m in the Antarctic ice near the geographical South Pole (see figure 3.1). The planned extension to AMANDA is "IceCube". It will be placed at the same location, and consist of 4800 OMs on 80 strings (see figure 3.2). The proposed shape is roughly cylindrical, 950 m high and 1100 m in diameter. The instrumented volume will thus be ~1 km^3 – 60 times the volume of AMANDA-II. In these telescopes the neutrinos are detected indirectly through the charged particles produced in weak neutrino-nucleon interactions in the vicinity of the detector.

In the case of an incident muon neutrino reacting through the charged current weak interaction, a muon escapes this reaction vertex, emitting so-called Čerenkov radiation as it propagates through the detector medium (ice). This Čerenkov radiation can be regarded as an electro-magnetic analogy to the bow shock wave of a boat in water or the shock front accompanying supersonic flight (see figure 3.3). For a more detailed description of this phenomenon see e.g. [29].

The Čerenkov photons are emitted in a direction θ_C relative to the direction-of-propagation for the muon.

$$\cos\theta_C = \frac{1}{\beta \cdot n_{\text{ice}}(\lambda)} \ , \tag{3.1}$$

where $\beta = 1$ is the velocity of the muon and $n_{\text{ice}}(\lambda)$ is the refractive index of ice (where λ is the photon wavelength). The number of Čerenkov photons emitted by the muon per unit path length and unit wavelength is [18]

$$\frac{\mathrm{d}^2 N}{\mathrm{d}x\mathrm{d}\lambda} = \frac{2\pi\alpha}{\lambda^2}\left(1 - \frac{1}{\beta^2 n_{\mathrm{ice}}^2(\lambda)}\right) \quad , \tag{3.2}$$

where $\alpha = 1/137$ is the fine structure constant.

According to [30] the relevant wavelength interval for AMANDA (and IceCube) is limited by the wavelength dependent sensitivity of the photo sensors. Roughly speaking, only photons between $\lambda_1 = 300$ nm and $\lambda_2 = 600$ nm will be detected. In this wavelength interval the refractive index may be approximated by a constant value $n_{\mathrm{ice}} \approx 1.32$. Photons produced by the muon will therefore be propagating through the detector on a cone with a half opening angle of $(90° - \theta_C) \approx 49°$.

By registering the time of arrival of this cone to the individual OMs, the direction of the muon track may be reconstructed. Since the directional shift (mean angle) between neutrino and muon decreases with energy like E_ν^{-2} (due to the Lorentz-boost in the forward direction), with a pointing accuracy of ~1.5° at 1 TeV [31], the reconstructed track direction may serve as an estimate of the direction of the incoming neutrino.

To obtain the number of emitted photons per unit length one may now insert the constant value for the refractive index into equation (3.2) and integrate over the relevant wavelength interval

$$\frac{\mathrm{d}N}{\mathrm{d}x} = 2\pi\alpha \int_{\lambda_1}^{\lambda_2} \frac{\sin^2\theta_C}{\lambda^2}\mathrm{d}\lambda \quad . \tag{3.3}$$

The result is $\sim 3.3 \cdot 10^4$ photons/m (from the muon itself). However, this emission is only responsible for a small fraction of the total number of photons emitted along the muon path. Many other processes take place where the muon energy is lost to secondary particles that – in many cases – will also emit Čerenkov radiation. At low energies muon energy is lost mostly through ionization, but at higher energies radiative processes like emission of bremsstrahlung, e^+e^- pair production and muon hadronization dominate [18]. Since the secondary particles will travel in directions similar to that of the muon, equation (3.3) is still a valid expression for the emitted Čerenkov radiation along the muon track. However, in order to get the number of photons per unit length *all* relevant secondary particles along the track must be accounted for.

Above 1 TeV the total energy deposit per unit length of a muon track is roughly proportional to the muon energy (see equations 6.6 and 6.7). This enables the possibility to estimate this energy from the length of the reconstructed track segment within the detector volume and the number of detected photons. In AMANDA the energy resolution using this method is slightly better than one order of magnitude [31]. The reconstructed muon energy can thus be used to obtain a rough estimate for the energy of the parent neutrino.

If the incident neutrino reacts through the neutral-current weak interaction, or if the neutrino is of the electron or tauon flavor, there will not be a track-like signature. Instead a shower of particles will be produced near the neutrino-nucleon reaction vertex. This will be referred to as the cascade signature, and it is described further in chapter 5. Yet another signature that may occur is the double bang signature. It is the result of a charged current tau neutrino reaction, where the neutrino energy is ~1 PeV or higher. This signature may be described as two cascades separated by a tauon track. It is at focus in this thesis, and is described further in chapter 6.

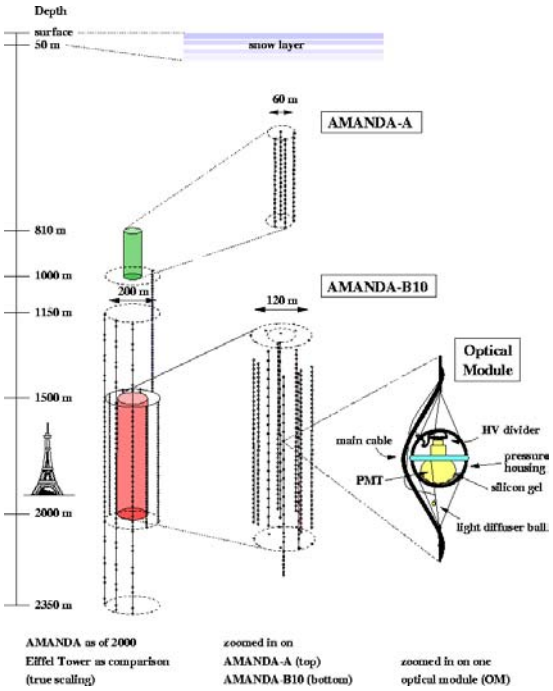

Figure 3.1 The AMANDA-II detector, deployed in the glacier ice near the geographical South Pole

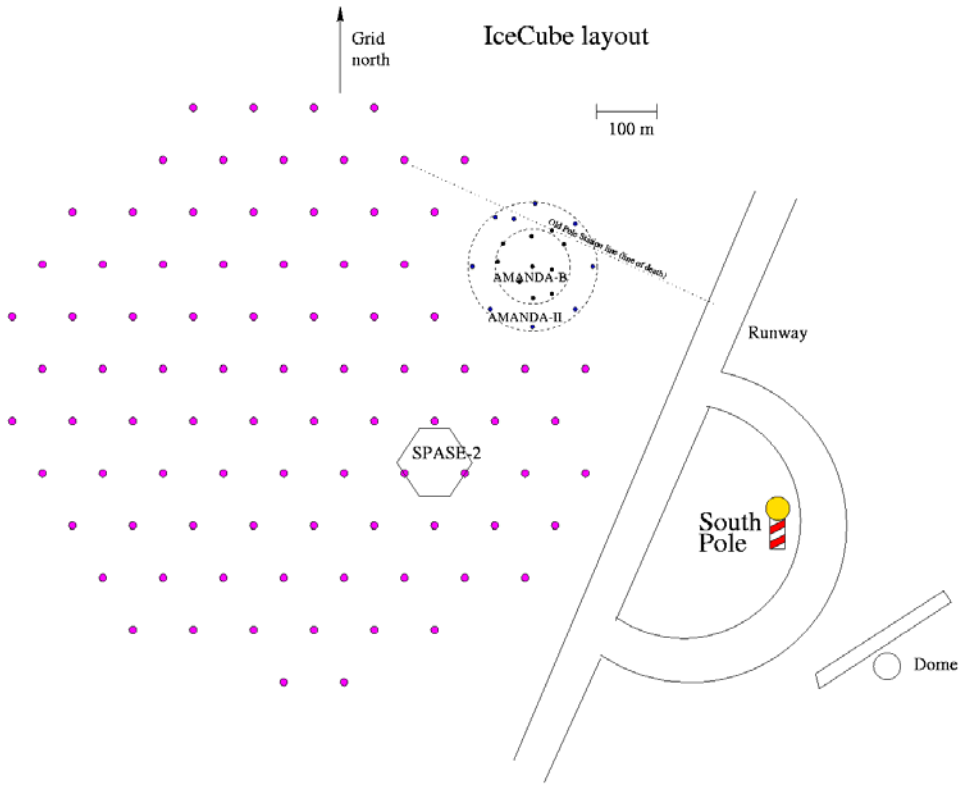

Figure 3.2 Top view of the IceCube detector, to be deployed in the glacier ice near the geographical South Pole

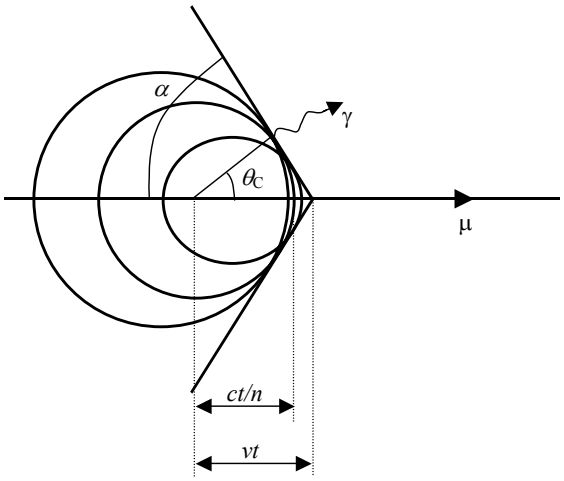

Figure 3.3 A qualitative illustration of the appearance of *Čerenkov* radiation as a charged particle (e.g. a muon) travels through a transparent medium at a velocity (v) exceeding the velocity of light (c/n) in that medium. θ_C is the emission angle with respect to the direction of propagation for the charged particle. α is half the opening angle for the Čerenkov cone. ct/n is the distance traveled by the photon since the time of emission (t), and vt is the distance traveled by the charged particle in the same time.

3.2 Ice properties

The optical properties of the detector medium are very important for the performance of the neutrino telescope. If photons are scattered, the Čerenkov cone will be deformed and information about the point of origin for the photons will be degraded. If the photon absorption in the medium is high OMs must be placed closer together than in a medium with less absorption to ensure that a sufficient number of OMs are illuminated in each event.

The scattering centers distributed in a glacier may be of at least two different types – air bubbles and dust grains. Bubbles are formed as air gets trapped in the accumulating snow at the surface. The snow gets buried and, in time, transforms to ice with the air present in the form of bubbles. At grater depths (older ice) the size of the bubbles is reduced due to the increasing pressure. Finally (at a certain pressure), a phase transition is possible where the air gets incorporated into the crystal structure of the ice. This is a slow process, and the depth where all bubbles have transformed depends on the local growth rate of the glacier. Below this depth scattering will be dominated by dust, which is typically distributed in horizontal dust layers.

Scattering is described quantitatively by the effective scattering length [32]

$$\lambda_e = \frac{\lambda_{geo}}{1 - \langle \cos\Theta \rangle} \quad , \tag{3.4}$$

where λ_{geo} is the average geometrical length between scatterings and Θ is the scattering angle. The average $\langle \cos\Theta \rangle$ is different for bubbles (0.75) and dust (0.8 – 0.9). Dust is therefore less serious from a scattering point of view.

Absorption can take place either in the ice itself or in dust grains or other substances, and is described quantitatively by the absorption length (average path length traveled before absorption) λ_a. In contrast to scattering the absorption is highly wavelength dependent.

Direct measurements of the effective scattering length and the absorption length have been performed for the South Pole ice at depths between 1400 m and 2300 m [33]. The investigation was done with pulsed and D.C. light sources buried at different locations in the ice, and with a laser at the surface sending pulses down optical fibers to diffusing nylon spheres embedded in the ice. The emitted light was registered by the surrounding OMs. The measurements show that the scattering due to bubbles is negligible at depths below ~1400 m. Below this depth scattering due to dust dominate, and several peaks in scattering appear at well defined depths (see figure 3.4).

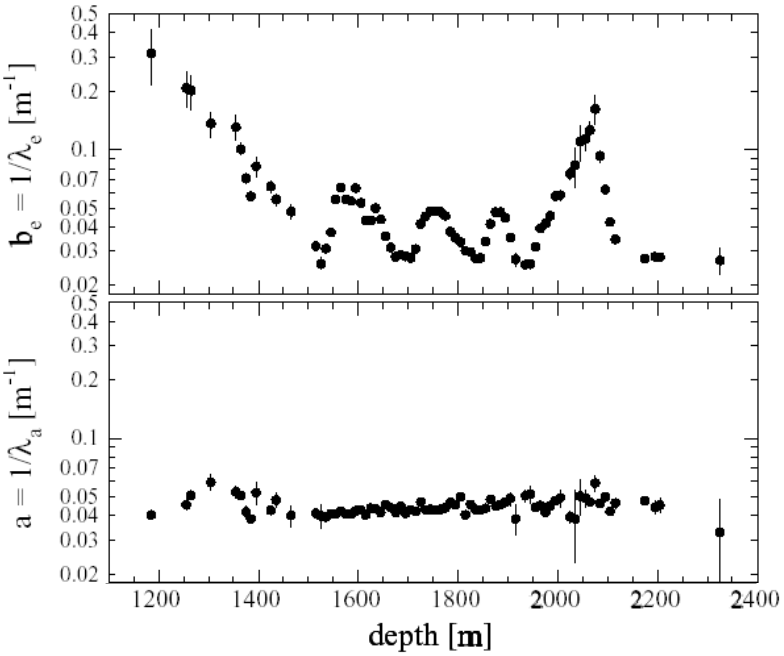

Figure 3.4 Optical properties of the South Pole ice – measurements of absorption coefficient $a(z) = 1/\lambda_a(z)$ and scattering coefficient $b(z) = 1/\lambda_e(z)$ at 532 nm (plots from [33]).

Besides the bulk ice, the ice along each string must be studied separately. This is the region of the former hole — drilled with hot water — into which the string of OMs with their accompanying cables were deployed. It has been shown that after refreezing this ice contains a lot of air in the form of bubbles, which originates from the glacier ice melted in the drilling process. This "bubbly" region may affect both the angular sensitivity of the OMs and the timing properties [34].

Laboratory freezing-experiments [35] [36] (the latter by myself) indicate that bubbles will be present even if measures are taken to remove some air from the water in the hole before it refreezes. Due to the poor solubility of air in ice, the air concentration in water will increase as the ice forms on the walls of the hole. Unless the water initially is completely devoid of air there will be a point where the concentration is high enough for bubbles to form on the inner surface of the hole. From this point onward bubbles will be trapped, resulting in a central core of "bubbly" ice (see figure 3.5).

Figure 3.5 Freezing of an ice cylinder (demonstration performed by myself). The picture on the left shows the "bubbly core", surrounded by clear ice. The picture on the right shows a partially frozen (hollow) cylinder, which illustrates some details of the freezing process (radial lines of bubbles outside the bubbly core).

3.3 Optical modules

The optical modules consist of a photo multiplier tube (PMT), 20 cm in diameter, contained in a spherical glass vessel. The "front end" of the PMT is positioned close to the inner surface of the vessel, where it is held in place by an "optical gel". The vast majority of the OMs were equipped with "Hamamatsu R5912-2" PMTs. These PMTs have 14 dynodes and are operated at a gain of ~10^9. This high gain is needed to be able to detect a pulse, induced by a single photo-electron, after ~2 km of cable.

The gain is controlled by the high-voltage (HV) settings used to accelerate the electron avalanche through the dynode chain. The HV values are set individually for each PMT, and should ideally remain unaltered after calibration. Any changes in voltage will change not only the gain but also the signal transit time.

The transit time is defined as the time from the emission of a photo-electron at the photo cathode to the time of appearance of the current pulse at the anode. The change in transit time (ΔT) for a change in HV from U_0 to U_1 may be evaluated with a phenomenological one-parameter model [37]

$$\Delta T = D \cdot \sqrt{\frac{2m_e}{q_e}} \cdot \left(U_1^{-1/2} - U_0^{-1/2} \right) , \tag{3.5}$$

where m_e and q_e is the mass and charge of the electron, and the effective length D is the model parameter. (Mathematically, equation (3.5) describes the change in transit times for electrons accelerated in the electric field between two parallel plates, separated a distance D.) In [37] the validity of this model was verified for one PMT resulting in good agreement for an effective length of D = 68.6 cm (see figure 3.6).

Figure 3.6 Shift in Transit Time as a function of applied PMT voltage (zero shift at normal operation). The *Effective Length D* is a model parameter that is most readily determined from experiment. The optimal least-square fit between model behavior (line) and measurements (dots) is found for D = 68.6 cm.

3.4 Signal transmission and amplification

Each PMT is connected to the surface via a cable, which has the double function of supplying the HV to the PMT and transmitting the photon-induced PMT pulses to the surface electronics. Three different types of cables have been used in AMANDA. For the first four deployed strings (numbered 1 – 4), coaxial cables were used. For strings 5 – 10 twisted-pair cables with a conductor diameter of 0.9 mm were used. The remaining strings, 11 – 19, were also equipped with twisted-pair cables, but with a conductor diameter of 0.7 mm.

The coaxial-cable solution proved to pick up very little noise, while the two twisted-pair solutions showed both more pick-up (signals picked up from the electronic environment) and more "white" noise. Also, "cross-talk" between different twisted-pairs within a string was observed [52]. In later strings (11 – 19) also an optical read-out for the PMT signal was introduced, thus reducing the function of the twisted pair to supplying the HV.

At the surface the HV is capacitively decoupled and the PMT signal is fed into an amplifier device named SWAMP (SWedish AMPlifier). Different versions of SWAMPs were used side-by-side in AMANDA, with essentially one SWAMP "flavor" for each type of cable. This device has three outputs:

- The "prompt" line (PL) carries the amplified signal.
- The "delayed" line (DEL) carries an amplified signal, delayed ~2 μs.
- The "direct" line (DIR) carries a test signal "tapped" before amplification. (DIR may also be used for *injecting* a test signal.)

The PL signals are connected both to the trigger system and to TDCs (Time to Digital Converters) used for retrieving the pulse widths. The TDC information is buffered and contains the last 8 pulses (8 leading edges and 8 trailing edges). The DEL signals are connected to peak-sensing ADCs (Analog to Digital Converters) used for retrieving the pulse amplitude information. The delay is needed to await the forming of the trigger, since the ADC information is *not* buffered.

3.5 The trigger

For every detector channel (corresponding to one OM) the PL signal from the SWAMP is connected to the trigger system. The PMT pulses are first converted in a discriminator equipment to logical trigger pulses, with a length of $T \approx 2$ μs. These pulses are then added in the DMADD (Digital Multiplicity ADDer) [32]. This equipment forms a trigger signal whenever the number of channels with overlapping trigger pulses meets or exceeds a certain multiplicity level (M). As the trigger "fires" the event information is stored for off-line analysis. The multiplicity level is selected as low as possible to allow short muon tracks and/or low-energy muons to trigger the detector without getting too high background trigger rate.

All PMTs spontaneously emit so-called "dark-noise" pulses, with a certain pulse rate f_{dn}. These pulses are responsible for a background trigger component. Background triggers occur when the number of overlapping trigger pulses due to dark noise accidentally meet the trigger condition. An expression describing this background trigger rate (f_{M}) for N channels has been derived in [38]:

$$f_M = \underbrace{\frac{M}{T}}_{A} \cdot \underbrace{\frac{N!}{M!(N-M)!} \cdot P^M \cdot (1-P)^{N-M}}_{B} \quad ; \quad P = f_{\mathrm{dn}} \cdot T \,. \tag{3.6}$$

Here, "A" is an approximation of $1/T_M$ where T_M is the average duration of an accidental M-fold coincidence event, and "B" is the probability to find the detector in an M-fold coincidence state (due to dark noise) at any given time. The validity of the expression was verified by a comparison with Monte Carlo simulations of a model detector with its trigger set at different multiplicity levels. The number of channels in the model detector was $N = 100$, all with a dark-noise frequency of $f_{\mathrm{dn}} = 2$ kHz. The result is presented in figure 3.7.

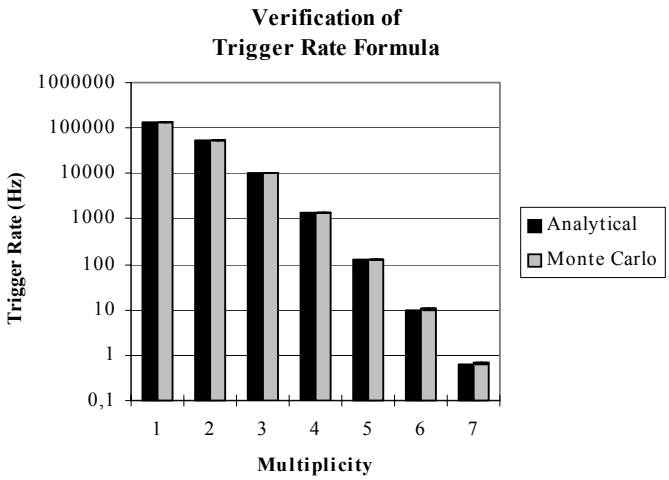

Figure 3.7 Comparison between trigger rates determined analytically and by using a simple Monte Carlo simulation program. The two sets of rates agree well. (Errors for MC data are ~within the line width.)

Chapter 4

Investigation of detector properties

4.1 Detector simulation with electra

4.1.1 Motivation

Monte Carlo simulation programs are used in AMANDA to study different aspects of the experiment. There are simulation programs that mimic the expected behavior of the sources for the particles that might be observed in the detector. These programs are often referred to as “generators”. Then there are simulation programs that mimic the behavior of the whole, or parts, of the detector itself. The standard simulation package for the simulation of the AMANDA telescope is called `amasim` [39].

`amasim` is, however, not the only program for electronics simulations in AMANDA; `electra` [40] was developed independently and in parallel by Staffan Carius and myself. This program is intended to be very realistic, incorporating as many of the known features of the equipment as possible. The intention is to simulate these features at a “fundamental” level, but some of them may have an alternative implementation at a ”phenomenological” level.

Since `electra` is not optimized for speed, this program was primarily intended as a tool for validating and refining other programs.

4.1.2 Description

The input to `electra` is the AMANDA configuration, which is read once, and the event information, which is supplied when calling `electra`. The configuration is defined in an OM database. The event information is a list of all photon hit-times for all OMs in an event.

When an event is initiated `electra` first determines the time interval to be simulated. This is defined as starting 5 μs before, and ending 15 μs after the earliest photon hit time. For this time interval the analog signals from all PMTs are simulated in 1 ns time steps.

For each PMT the simulation starts by generating different signal "features" that will eventually be combined to form the analog PMT signal. These features include electronic noise, different pulses from the PMT and cross-talk pulses. After combining all of these the pulse detection is simulated and the trigger conditions are checked. If a trigger is obtained the ADC (peak amplitude) and TDC (leading and trailing edges) information is extracted. An outline of the program structure is presented in figure 4.1.

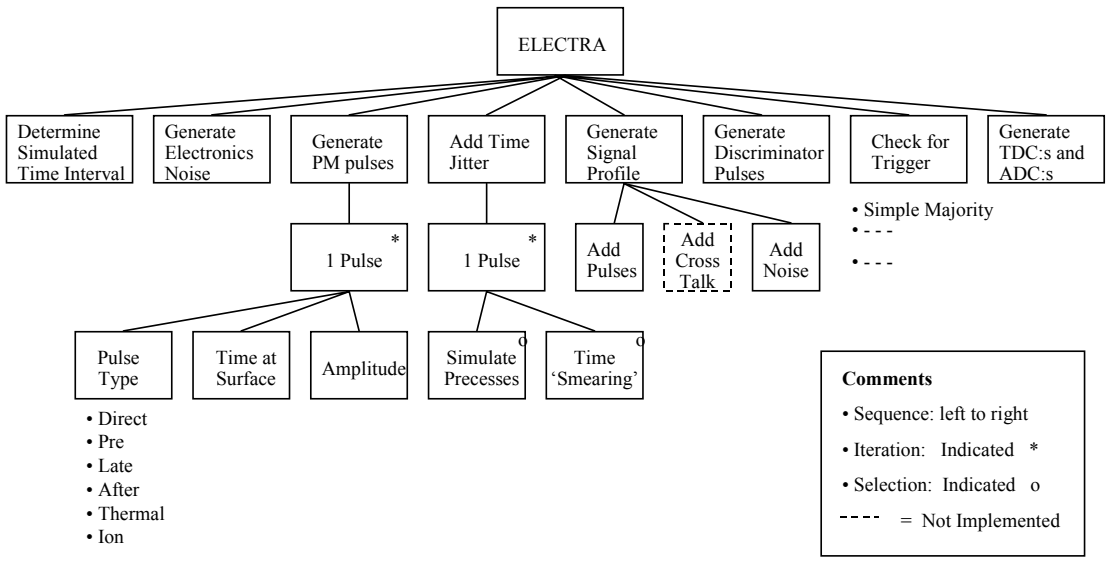

Figure 4.1 An outline of `electra`, a program for simulating the detector electronics in AMANDA.

4.2 An all-channel survey for AMANDA-B13

4.2.1 Introduction

During the austral winter the AMANDA telescope is taking data, and one does not want to interrupt this process without having strong reasons to do so. Therefore not all details of the detector can be monitored continuously, and if problems occur during the season they might elude an early discovery. To be able to take full advantage of the data taken during the year it is therefore important to perform diagnostic measurements on the detector as soon as the *Amundsen-Scott South Pole Station* opens for the summer.

For the austral summer of 1999 – 2000 major changes were scheduled for AMANDA. New strings were to be deployed and the detector electronics were to be upgraded. During one month in November and December 1999, prior to the scheduled changes, I was responsible for several investigations performed to be able to describe the status of the electronics in AMANDA-B13 and to identify problematic detector channels. The main effort was put into the early stages of the signal chain.

All acquired information is presented in the report [41]. In the following sections some of the results are presented as a survey over the investigated detector properties.

4.2.2 High voltage settings

One fundamental requirement for a working detector channel is that its PMT is powered with an appropriate high voltage (HV). In AMANDA-B13 three power-supply units are used to support all its PMTs:

	Channel Range	Name of Unit
First crate:	HV channels 0-255	LeCroy 1440/M1 (M1=Mainframe 1)
Second crate:	HV channels 256-511	LeCroy 1440/M2 (M2=Mainframe 2)
Third crate:	HV channels 512-703	LeCroy 1458

The HV settings were obtained using HV-channel printouts from the power supplies themselves, thus guaranteeing an up-to-date listing of the voltages. In figure 4.2 these voltages are presented in a *voltage* versus *OM-number* plot.

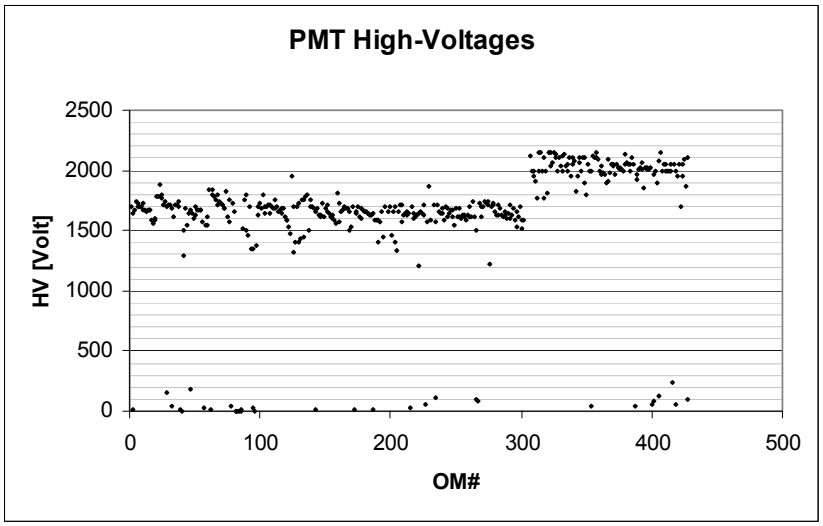

Figure 4.2 Overview of all PMT HV-settings (the actual voltages) in AMANDA. OM numbers in the range 1-86 are associated with strings 1-4, OM numbers in the range 87-302 are associated with strings 5-10, and OM numbers in the range 303-428 are associated with strings 11-13. Disregarding channels with very low voltage (<500 V), the average voltage for PMTs in strings 1-4 is 1685 V, for PMTs in strings 5-10 the average voltage is 1635 V, and for PMTs in strings 11-13 it is 2021 V. 419 PMTs are connected to a HV channel. 33 of these have very low voltages and are therefore inoperable.

The result of a closer inspection can be summarized as follows:

- 419 of the PMTs with an OM number in the range 1 – 428 are connected to a HV channel.
- 33 of these PMTs have very low voltages (<500 V) and are therefore inoperable.
- The average voltage for PMTs in *strings 1 - 4* is ~1685 V (disregarding channels with very low voltages).
- The average voltage for PMTs in *strings 5 - 10* is ~1635 V (disregarding channels with very low voltages).
- The average voltage for PMTs in *strings 11 - 13* is ~2021 V (disregarding channels with very low voltages).

The higher HV setting for strings 11 – 13 will result in a higher gain*. According to [42] PMTs in strings 1 – 4 (connected to coaxial cables) are operated at a gain of $1.5 \cdot 10^9$, PMTs in strings 4 – 10 (connected to 0.9 mm diameter twisted pair cables) are operated at $0.8 \cdot 10^9$ and PMTs in strings 11 – 13 (connected to 0.7 mm diameter twisted pair cables) are operated at $3.4 \cdot 10^9$. The objective is to drive a 1 photo electron signal over ~2 km cable, and the different gain requirements reflect differences in cable and PMT properties. Table 4.1 presents the batch-dependent HV-settings corresponding to a $1.0 \cdot 10^9$ gain [42].

Strings	HV
1 – 4	1618 V
5 – 10	1684 V
11 – 13	1771 V

Table 4.1 Batch-dependent HV-setting corresponding to a $1.0 \cdot 10^9$ gain

Another feature revealed in figure 4.2 is a distribution in the HV settings within each string. This is explained by individual variations in the PMT properties, and by the fact that PMTs deployed at greater depths will require a higher gain to overcome the higher attenuation. However, the distribution in PMT properties is used to reduce the differences in HV settings within a string. Thus, the most "effective" PMTs are deployed at the greatest depths.

4.2.3 Pulse rates

In the DMADD trigger system, the multiplicity of an event is not obtained in one step. Instead, first a "local" multiplicity is determined for a subgroup of up to 20 channels, connected to a so-called MULT20 module. The multiplicities from all subgroups are then combined in a PREADDER/ADDER sequence to form the "global" multiplicity.

* PMT gain is defined at the number of electrons produced at the anode as a response of a single photo electron.

On the front of each MULT20 module it is possible to monitor the discriminated pulses for channels connected to that module. For each channel in the AMANDA-B trigger system the following measurements were performed:

- The signal was connected to a scaler where the number of pulses was counted for one minute, thus determining the pulse rate for that channel.
- The signal was connected to a digital oscilloscope where the pulse width was measured.
- Pulse rate, pulse width and comments about any "strange behavior" were noted.

In figure 4.3 these measurements are presented in a *pulse width* versus *pulse rate* plot. The result of a closer inspection can be summarized as follows:

- 374 channels were connected to the DMADD system.
- 9 channels had very low pulse rates (f <100 Hz)
- 11 channels had very high pulse rates (f > 3000 Hz).
- 5 channels were not stable (intermittent signal).
- 46 channels were found to be "silent", i.e. they showed no signal at their test outputs.
- Typical pulse rates were ~300 Hz (strings 1 – 4) or ~1300 Hz (strings 5 - 13).
- Pulse widths were distributed between 2.0 μs and 2.7 μs.

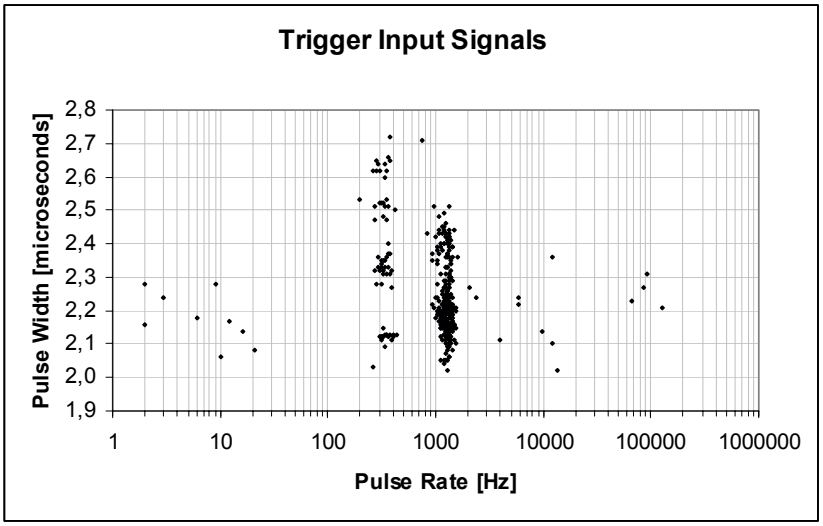

Figure 4.3 The discriminated pulses from 374 channels in strings 1 – 13 were used as input to the AMANDA-B trigger. Both pulse rates and pulse widths were measured at the test outputs on the front of the MULT20 modules. Typical pulse rates were ~300 Hz (strings 1 – 4) or ~1300 Hz (strings 5 - 13), and the pulse widths were distributed between 2.0 μs and 2.7 μs. 46 channels were found to be "silent", i.e. they showed no signal at their test outputs.

A large fraction of the PMT background pulse rates is believed to be due to exposure from radioactive material in the spherical glass vessels that are used for housing the PMTs. Measurements of the content of different radionuclides in the glass is presented in the report [43]. The type of vessel used in strings 5 – 13 (BENTHOS) was found to contain significant amounts of uranium, thorium and potassium (U, Th, K). The type of vessel used in strings 1 – 4 (BILLINGS) was found to contain similar amounts of U and Th but only about 4% as much K compared with the BENTHOS spheres. It is therefore believed that the difference in the amount of K in the two types of glass vessels is the probable cause for the observed difference in pulse rates (see figure 4.3).

In [42] the pulse rates are used together with the corresponding HV settings to calculate the amount of charge leaving the anode of PMTs in different strings. The annual anode charges thus obtained are 0.9 C for strings 1 – 4, 1.6 C for strings 5 – 10 and 7 C for strings 11 – 13. These numbers are important since the lifetime of a PMT is limited by the total integrated charge. For the PMTs used in AMANDA a 50% gain drop (at constant HV) is expected for an integrated charge of ~115 C [42].

4.2.4 Pulse shapes

One important "tool" for diagnosing the operation of a SWAMP (and the PMT connected to it) is to look for any strange features in the shape of its PMT pulses. With the experience from looking at many signals I formed a subjective opinion about what "normal" pulses should look like. A few channels with pulses falling into this category were selected. For each channel a number of pulses were digitized at the prompt line (using a 500 MHz digital oscilloscope) to be used as reference pulses.

In figure 4.4, a selection of the digitized pulses is presented. In these plots a couple of pulse-shape features may be noted, which appear in a systematic manner: First, as expected, the pulse widths are larger for PMTs deployed at greater depths, since these channels are equipped with longer cables. Secondly, in strings 11 – 13 we observe a clear difference between the pulse shapes from odd numbered PMTs (position number in the string) compared with even numbered ones. In the "odd" case one sees a "kink" on the trailing edge of all pulses, which is not observed for "even" channels. The cause of this effect has not been determined, but one suggestion is that it is due to signal reflections in the connector for the "pigtail" connecting every odd-numbered OM to the cable near its position in the hole.

In addition, when comparing pulses, one should be aware of that due to development over the years different cables as well as different versions of SWAMPs have been used. In November 1999 three "generations" of cable/SWAMP combinations were used, with slightly different pulse shapes. The three generations are defined as:

- Generation 1: Strings 1 – 4 (OMs 1-86)
- Generation 2: Strings 5 – 10 (OMs 87-302)
- Generation 3: Strings 11 – 13 (OMs 303-428)

The pulse shapes are described using the set of digitized pulses mentioned above. To characterize the pulses four parameters are used:

- ΔT_{LE}: "Rise time" of leading edge (10% to 90%).
- ΔT_{TE}: "Fall time" of trailing edge (90% to 10%).
- ΔT_{FWHM}: Full width at half maximum (FWHM).
- $R = A_{os}/A_P$: Relative overshoot amplitude (overshoot_amplitude / pulse_amplitude).

For generations 1 and 2, two channels were investigated in each case, one with its PMT near the top of the instrumented section of a string, and one with its PMT near the bottom. For generation 3 also one channel in the middle was selected since the corresponding strings have longer instrumented sections. The parameter values for the three generations at different depths are presented in table 4.2.

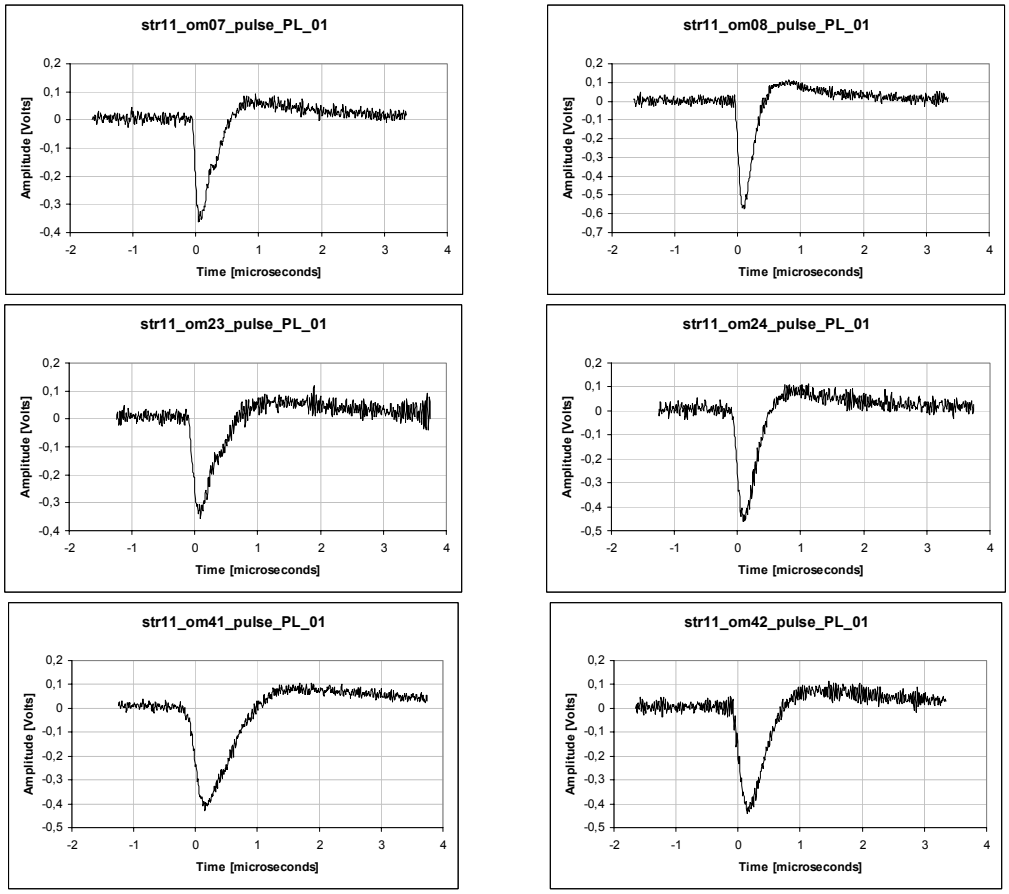

Figure 4.4 A few "typical" PMT pulses digitized from the prompt line of channels in string 11. This string uses twisted pair cables. Increasing OM number indicates increasing cable length. The pulse width increases with increasing cable length. Note also an OM-number odd/even effect for the pulse shapes.

Generation	Str #	OM #	# Pulses	$\langle \Delta T_{LE} \rangle$ [ns]	$\langle \Delta T_{TE} \rangle$ [ns]	$\langle \Delta T_{FWHM} \rangle$ [ns]	R [%]
1	??	Top	10	125.6 ± 1.2	309.4 ± 1.7	351.4 ± 1.9	35.87 ± 0.36
1	??	Bottom	10	180.0 ± 2.9	372.7 ± 3.7	464.8 ± 3.0	43.32 ± 0.27
2	07	01	9	51.56 ± 0.67	152.7 ± 2.6	145.1 ± 1.4	24.70 ± 0.30
2	07	35	8	66.2 ± 1.6	149.6 ± 2.3	164.1 ± 1.7	28.22 ± 0.62
3	11	11	9	86.8 ± 2.6	244.2 ± 6.0	222.7 ± 3.0	23.13 ± 0.80
3	11	24	6	119.0 ± 5.0	302.0 ± 9.7	286.0 ± 6.9	24.68 ± 0.41
3	11	42	6	163.8 ± 8.7	431.3 ± 7.2	385 ± 10	26.0 ± 1.2

Table 4.2 Pulse shapes for channels belonging to the three different "generations" have been digitized. The files were used to extract four characteristic numbers: The "rise time" of the leading edge, ΔT_{LE} , the "fall time" of the trailing edge, ΔT_{TE} , the pulse width (Full Width at Half Maximum), ΔT_{FWHM} , and the relative magnitude of the positive overshoot compared with the amplitude of the leading negative pulse, R. In the table the mean values for the given number of pulses are presented. Channels at different depths were investigated. (Higher OM # indicates greater depth within a string.) For the two channels from generation 1 (in strings 1-4) the string and OM numbers have unfortunately been lost. However, the "Top" and "Bottom" labels are valid.

4.2.5 Noise, cross-talk and external pick-up

A problem that has been observed is that channels are not always completely isolated (electro-magnetically) from each other. This manifests itself in very short *cross-talk* pulses appearing in one channel in coincidence with normal PMT pulses in another channel. A few cross-talk pulses were digitized, and one example is presented in figure 4.5. Typically a cross-talk pulse is ~9 ns wide (FWHM) in the DIR output, but widens to ~33 ns (FWHM) in the PL output.

Apart from cross talk, also *white noise* and different types of *pick-up* signals have been noted in many channels. More "rare" noise features include *baseline shifts* and *doublet pulses*.

Noise, and pick-up signals are less prominent in strings 1 – 4 (generation 1), since these channels use coaxial cables, which are better shielded than the twisted pair cables used in rest of the detector.

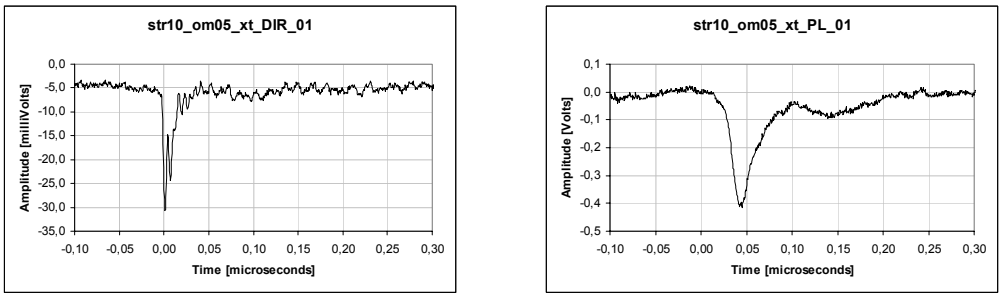

Figure 4.5 A "typical" cross-talk pulse (from a channel in string 10) is shown as it appears on direct line and prompt line respectively. The direct pulse is ~9 ns wide (FWHM), and the prompt pulse is ~33 ns wide (FWHM).

4.2.6 SWAMP gain and delay

The amplitude gains in PL and DEL outputs, and the delay between PL and DEL outputs were measured for all operational SWAMPs. In order to do so the following set-up was assembled: A pulse generator was used to produce test-pulses with a shape similar to PMT-pulses as they appear in the DIR output. The pulse shape (after attenuation) was measured with a digital oscilloscope to have the following characteristics (negative pulses):

DC Offset:	2 mV
Leading Edge Fall-Time:	100 ns
Trailing Edge Rise-Time:	186 ns
Width (FWHM):	220 ns
Amplitude:	12.6 mV

This signal was connected to a lemo-T thus splitting the signal to the oscilloscope (1 MΩ termination) and the Direct Line of the SWAMP, which was now used as an injection point. The Prompt and Delayed outputs from the SWAMP were connected to two other inputs on the oscilloscope (50 Ω termination).

For each SWAMP the amplitudes of the injected signal, A_{TST}, the prompt signal, A_{PL}, and the Delayed signal, A_{DEL}, were measured. The PL-gain was defined as $G_{PL} = A_{PL}/A_{TST}$, and the DEL-gain was defined as $G_{DEL} = A_{DEL}/A_{TST}$. (Note the fundamental difference between these gain definitions and the PMT gain, which specify the number of electrons leaving the anode for each initial photo electron.) The SWAMP-delay ΔT was measured between the starting points* of the pulses in PL and DEL.

These measurements (PL-gain, DEL-gain and SWAMP-delay) yield the status of the SWAMP performance, without depending on the presence of "good looking" PMT pulses. The measurements are presented in two plots: Figure 4.6 shows G_{DEL} versus G_{PL}, and figure 4.7 shows the ΔT distribution.

* The starting point of a pulse was found by eye extrapolating the leading-edge slope back to the point where it would cross the signal base line.

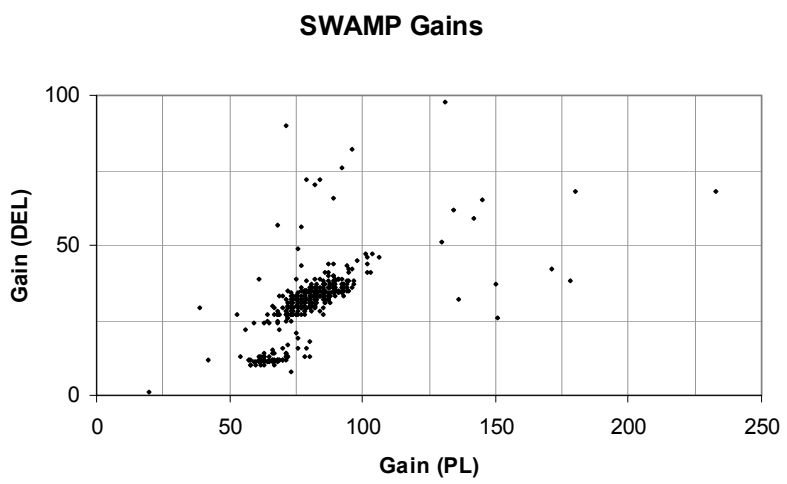

Figure 4.6 Two versions of the amplified PMT signal are available on different SWAMP outputs. The *prompt* signal is used for extracting time information and for trigger purposes. The *delayed* signal is used for extracting amplitude information. Presented here is the gain distribution for the two outputs (delayed vs. prompt). Typical gains were [G_{PL}≈60, G_{DEL}≈10] (strings 1 – 4) or [G_{PL}≈80, G_{DEL}≈35] (strings 5 – 13). The total number of SWAMPs was 442. 35 of these were found to be "dead", i.e. they showed no signals at the amplified outputs. One was "semi-dead", with signal in prompt but not in delayed output.

The result of a closer inspection can be summarized as follows:

- The total number of SWAMPs was 442
- One SWAMP showed two almost identical pulses in the DEL output. (The first pulse was in coincidence with the pulse in the PL output; the second had a "normal" delay.)
- One SWAMP showed signal in PL but not in DEL.
- 35 SWAMPs were found to be "dead", i.e. they showed no signals in PL and DEL.
- Typical gains were [G_{PL}≈60, G_{DEL}≈10] (strings 1 – 4) or [G_{PL}≈80, G_{DEL}≈35] (strings 5 – 13).
- Almost all SWAMPs had a delay somewhere between 2.00 μs and 2.17 μs. (One channel singled out with a delay of 1.05 μs.) The average delay was 2.09 μs.

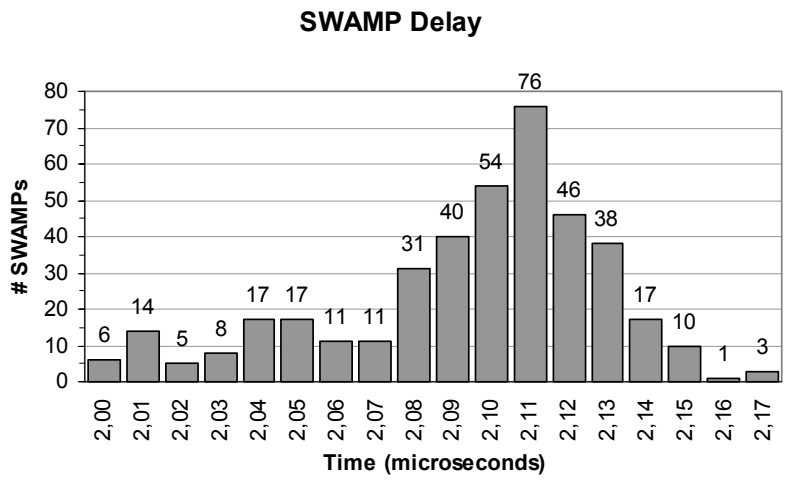

Figure 4.7 Two versions of the PMT signal are available on different SWAMP outputs. The *prompt* signal is used for extracting time information and for trigger purposes. The *delayed* signal is used for extracting amplitude information. Here is the distribution of delay times between these two outputs. (Note: One SWAMP with a delay of 1.05 μs is "out of scale" in this plot.) The total number of SWAMPs was 442. 35 of these were found to be "dead", i.e. they showed no signals at the amplified outputs. One was "semi-dead", with signal in prompt but not in delayed output. The mean delay was 2.09 μs.

Chapter 5

Cascade-like events

5.1 Intrinsic cascade properties

5.1.1 General properties

In the experimental data from AMANDA two types of event signatures may be identified using present day algorithms, *tracks* and *cascades*. The physical origin of the track signature is events where a charged particle propagates through a substantial part of the detector at a relativistic speed, while emitting Čerenkov radiation (see section 3.1). The origin of the cascade signature is events where an initial particle gives rise to extensive particle production at essentially a single point within or in the vicinity of the detector. These cascade events are initiated either when the initial particle reacts with the detector medium (ice) or when the particle decays in flight.

In chapter 10 a method is outlined for energy calibration of neutrino telescopes with respect to cascade events. Relevant cascade properties in this context are e.g. the geometry of these events, in particular their longitudinal development, and the amount of photons produced.

It should be noted that cascades are not exactly pointlike but *do* have a longitudinal extension - a *length* - in the direction of the velocity of the initial particle. This length is essentially proportional to the logarithm of the energy. Thus, the assumption that cascades are point-like is only valid if the energy deposit is not too high. Typical cascade lengths in water for cascades of a few PeV (representative for the events at focus in this thesis) lie between 10 m and 20 m [44] [45]. (The corresponding lengths in ice are obtained by multiplying by the density ratio $\rho_{water}/\rho_{ice.}$) After this distance only a small fraction of the initial energy remains to be deposited. These lengths are comparable to the distances between optical modules both in AMANDA-II and in IceCube (see section 3.1). Since the present reconstruction algorithms for cascade events assume that cascades are point-like it is possible that these algorithms will have to be modified to be able to support reconstruction of ultra-high energy cascades.

In calorimetric measurements of cascade events the signal amplitude obtained through the detection/analysis process should *ideally* be proportional to the number of photons produced. (Insufficient sampling in space will introduce a component of statistical uncertainty.) On average the number of photons produced in a cascade is proportional to the energy deposit, but since the particle production in cascades is a stochastic process there will, in general, be statistical fluctuations in the event-to-event number of photons per unit energy [45].

Furthermore, since the amount of photons produced per unit energy depends on the nature of the initial particle, the particle type (or at least the a priori probabilities for different particle types) should be known to enable the calculation of the energy deposit in a cascade event.

5.1.2 Electromagnetic cascades

The initiators for electromagnetic cascades are electrons and photons, but neutral pions may also be placed in this group of initiators due to their "prompt" decay into two photons.

There are two main processes that govern the development of an electromagnetic cascade, the production of a bremsstrahlung photon when an electron or a positron is accelerated in the field of a nucleus, and the conversion of a photon into an electron-positron pair. The result of these alternating processes is an "avalanche" of increasing numbers of electrons/positrons and photons. However, for each new "generation" the energy of the "daughter" particles will be lower than the energy of the "parent" particle. Eventually the electron energies will begin falling below a certain critical energy. The particle production stops and the cascade dies out [18].

Along the longitudinal development of the cascade electrons and positrons will emit Čerenkov photons. The number of photons will be roughly proportional to the total track-length of all charged particles participating in the cascade. For electromagnetic cascades the event-to-event fluctuations in the number of photons produced for a given energy E of the initiator particle is very small. GEANT [46]-based simulations performed for the BAIKAL experiment [44] have shown that the total track-length for an electromagnetic cascade in water is approximately

$$L(E) = (E/1\,\mathrm{GeV}) \cdot 4.89\ \mathrm{m} \tag{5.1}$$

For the wavelength interval where the PMTs are sensitive (300-600 nm) the photon yield in ice is $\sim 3.30 \cdot 10^4$ photons/m track [30], but since the number of Čerenkov photons for non-relativistic particles is smaller, the average yield is reduced. For electromagnetic cascades in water this correction factor was found to be 0.894 [44]. Thus, neglecting the difference in density between the detector medium at the BAIKAL and AMANDA/IceCube sites, electromagnetic cascades are expected to produce $\sim 1.44 \cdot 10^5$ (detectable) Čerenkov photons per GeV.

5.1.3 Hadronic cascades

With hadronic initiators the development of the cascades is more complex than in electromagnetic cascades, but since the basic interactions are well understood the particle production may be studied using Monte Carlo simulations.

As the cascade develops, secondary (charged) particles will emit Čerenkov radiation. There are, however, a couple of differences between hadronic and electromagnetic cascades that must be considered. On average hadronic cascades produce less amounts of photons compared with electromagnetic cascades, and the event-to-event fluctuations are larger, given the same incident energy.

The reason for the lower average number of photons is that energy is lost to low-energy neutrons and to the breaking of nuclei (binding energy). The reason for the larger fluctuations is that neutral pions amount, on average, to one third of the produced pions, and the energy carried by these neutral particles is deposited as electromagnetic cascades with a higher photon yield. The number of produced neutral pions early in the development of the cascade will therefore have a large impact on the total number of photons produced.

The GEANT-based simulations for the BAIKAL experiment [44] have shown that, on average, the total track-length for a hadronic cascade is approximately

$$L(E) = (E/1\,\mathrm{GeV}) \cdot 4.08 \text{ m}. \tag{5.2}$$

The photon yield is $\sim 3.30 \cdot 10^4$ photons/m track [30] times a correction factor of 0.86 [44]. Thus, if the difference in density between the detector medium at the BAIKAL and AMANDA/IceCube sites is neglected, hadronic cascades are expected to produce $\sim 1.16 \cdot 10^5$ Čerenkov photons per GeV (average value). This is about 80% of the photon yield in electromagnetic cascades.

5.2 Cascade detection

5.2.1 Introduction

Two reconstruction methods for cascades have been developed for the AMANDA-B10 detector [47], where cascades are regarded as point-like bursts of light with very short duration. A mathematical model is used for describing the emission, absorption and scattering of Čerenkov photons. The directions of the emitted photons are peaked at the Čerenkov angle with respect to the direction of the velocity of the cascade initiator particle.

5.2.2 Reconstruction of position and time

The first reconstruction method is used for determining the *position* and *time* of a cascade event. From the Čerenkov model a probability distribution $p(t_{\text{del}}, d)$ is derived for the expected "time delay" (t_{del}) between the observed photon *hit time* on an OM – at a distance *d* from the cascade – and the expected hit time without scattering:

$$t_{\text{del}} = t_{\text{hit}} - t_{\text{event}} - d / c_{\text{ice}} \tag{5.3}$$

A likelihood function is then constructed for all observed hit-times in an event

$$\mathcal{L} = \prod_{i=0}^{N_{\text{hits}}} p\left(t_{\text{del}}^{i}, d_i\right) \quad , \tag{5.4}$$

and the cascade parameters (position and time) are varied until the values corresponding to the maximum likelihood have been found.

5.2.3 Reconstruction of energy and direction

The second reconstruction method is used to obtain the *energy* and *direction* of a cascade. It uses the following expressions for the probabilities for a given OM to *observe* or *not observe* a signal from Čerenkov photons:

$$P_{\text{hit}} = 1 - e^{-\eta} \tag{5.5a}$$

$$P_{\text{no\_hit}} = e^{-\eta} \tag{5.5b}$$

The number of photons (η) hitting an OM is proportional to the energy of the cascade [44], and also depends on the cascade direction and the vector that joins the cascade vertex and the OM. A functional form of η has been determined, thus making it possible to construct the likelihood function

$$\mathcal{L} = \prod_{\text{hit\_OMs}} P_{\text{hit}} \times \prod_{\text{no\_hit\_OMs}} P_{\text{no\_hit}} \quad . \tag{5.6}$$

Since the position of the cascade vertex may be determined by the reconstruction method described in section 5.2.2 the energy and direction of the cascade are the only remaining free parameters in (5.6). These parameters are varied until the values corresponding to the maximum likelihood have been found.

5.2.4 Reconstruction performance

To extract cascade-event *candidates* each event detected with AMANDA is submitted to a selection algorithm, which selects events with certain properties presumed to be characteristic for cascade events. In [47] an investigation of the performance of these reconstruction methods is presented for the AMANDA-B10 detector (including simulation, selection and reconstruction of cascades). It shows that the expected energy resolution is ~45% in ($\log_{10}E_\nu$ - $\log_{10}E_{\text{C}}$) in the range 3 TeV < E_ν < 10 TeV, Here, E_ν denotes the *true* energy of an *electron neutrino* initiating the cascade, and E_{C} denotes the *reconstructed* cascade energy.

The investigation also shows that the expected position resolutions differ between coordinates in the horizontal plane (x and y) and the vertical coordinate (z): The r.m.s. values for the error distributions in reconstructed coordinates are 17.8 m for the x and y coordinates and 7.1 m in the z coordinate.

In a later paper [48] a similar investigation was done for AMANDA-II. For simulated mono energetic cascades ($0.1\,\mathrm{TeV} \leq E_\nu \leq 100\,\mathrm{TeV}$), distributed within the detector, the position resolution was in the order of 5 m. The energy resolution was 0.1 – 0.2 in $\log_{10}(E_C/1\mathrm{PeV})$.

In chapter 10 an energy calibration method for cascades is described using so-called double bang events (see section 6.1), where two cascades are produced within the detector volume. The potential for this method relies on the possibility to reconstruct the position (and time) of both of these cascades, and the energy of one of them. Since no attempt has been made to design a reconstruction algorithm for these events the performance of the single-cascade reconstruction in AMANDA-II will be used as an example of what might be possible to obtain for cascades in double bang events in the future.

Chapter 6

Detection of tau neutrinos

6.1 The double bang signature

6.1.1 Overview

One characteristic signature for tau neutrino reactions that might be observed in neutrino telescopes, like AMANDA or IceCube, is the so-called *double bang* signature: two large cascades separated in space and time by a tauon traveling close to the speed of light.

This signature occurs in a subset of the possible reaction schemes between a tau neutrino and a nucleon. The first "bang" is the hadronic cascade produced in a charged current reaction between the neutrino and a nucleon in the target material (ice). From this reaction a tauon emerges, emitting Čerenkov radiation as it propagates through the material. Eventually, the tauon decays and, depending on the nature of its daughters, a second cascade (the second bang) might occur, thus finalizing the signature (see figure 6.1).

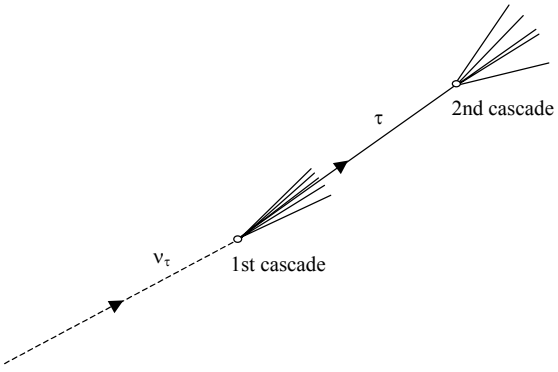

Figure 6.1 The *double bang* signature — two large cascades separated in space and time by a relativistic tauon — is a characteristic signature for a tau neutrino interacting with a nucleon.

The detection of double bang events in large neutrino telescopes is discussed in [7]. It is suggested that due to their unique signature there will probably be almost no background to these events. In this context, the word "background" refers to events that can fake the double bang signature. The most serious background contribution will, according to [7], be muon neutrino charged current events where the muon travels approximately 100 m before loosing most of its energy in a single bremsstrahlung reaction.

The fraction of muon neutrino charge current events having a signature similar to this is expected to be of the order $3 \cdot 10^{-3}$. In section 9.5 this number will be used to estimate the signal-to-background ratio in the AMANDA-II and IceCube detectors due to these background events.

6.1.2 The neutrino-nucleon reaction

Tau neutrinos (ν_τ) interact with nucleons (the isoscalar nucleon: $N = \frac{p+n}{2}$) through one of the following weak-interaction schemes:

- Charged current (CC) reaction: $\nu_\tau + N \xrightarrow{\text{CC}} \tau + \text{"}anything\text{"}$
- Neutral current (NC) reaction: $\nu_\tau + N \xrightarrow{\text{NC}} \nu_\tau + \text{"}anything\text{"}$

For both of these, energy is transferred to the struck quark of the target nucleon causing the nucleon to break. The result is a hadronic cascade. The fraction of the neutrino energy that is transferred to the quark is called the inelasticity of the reaction and is denoted by *y*. For the charged current reaction

$$y = 1 - \frac{E_\tau}{E_\nu} \tag{6.1a}$$

where E_ν is the energy of the incident neutrino and E_τ is the energy of the tauon produced in the reaction. For the neutral current reaction

$$y = 1 - \frac{E'_\nu}{E_\nu} \tag{6.1b}$$

where E'_ν is the energy of the neutrino escaping from the reaction vertex.

The cross sections for these two reaction schemes depend on the internal structure (quark content) of the nucleon. Each nucleon consists of three so-called "valence quarks" determining the electric charge (*proton*: $uud \Rightarrow Q_p = +1e$. *neutron*:$udd \Rightarrow Q_n = 0$), but in addition virtual quark/anti quark pairs are produced and annihilated continuously "inside" the nucleon. These virtual quarks are called "sea-quarks", and are available for reactions with e.g. neutrinos. The quark content may be described in terms of the so-called parton distributions, $q_f(x)$. The Bjorken scaling variable *x* is the fraction of the four-momentum of the nucleon carried by a single parton (quark). Thus $q_f(x)\mathrm{d}x$ is the expectation value of the number of quarks of flavor *f* in the nucleon whose four-momentum lies in the interval [*x*,*x*+d*x*]. The corresponding parton distributions for antiquarks are denoted by $\bar{q}_f(x)$.

The parton distributions are not known from first principles but have to be determined from experiments. In high-energy reactions the small-x quarks makes an important contribution to the cross-section. However, the small-x region has not been completely "mapped out" yet. Instead when trying to estimate the cross-sections for these reactions one has to rely on extrapolations of parameterized models of the parton distributions. One modern set of models for parton distributions is named CTEQ4-DIS [49]. The calculated cross sections for deeply inelastic neutrino-nucleon scattering (at neutrino energies between 10^9 eV and 10^{21} eV) using these distributions are presented in [22].

6.1.3 The tauon propagation

A tauon has a very short mean lifetime [18]

$$t_\tau = (290.6 \pm 1.1) \cdot 10^{-15} \text{ s.} \qquad (i)$$

This corresponds to a mean range of only

$$ct_\tau = (87.12 \pm 0.33) \cdot 10^{-6} \text{ m} \qquad (ii)$$

for a particle traveling close to the speed of light. However, for the most energetic neutrino reactions the emerging tauons will be extremely relativistic, and due to time dilation the observed mean range (R) in the *lab frame* is proportional to the gamma factor (γ):

$$R(E_\tau) = \gamma \cdot ct_\tau = \frac{E_\tau}{m_\tau c^2} \cdot ct_\tau \ , \qquad (6.2)$$

where the tauon rest mass is [18]

$$m_\tau = 1777.03^{+0.30}_{-0.26} \text{ MeV}/c^2 \ . \qquad (iii)$$

By inserting (*ii*) and (*iii*) into equation (6.2) one obtains a simple expression that will be used in the following chapters:

$$R(E_\tau) \approx 49 \text{ μm} \cdot \left(\frac{E_\tau}{1 \text{ GeV}} \right) \qquad (6.2')$$

Thus, for tauon energies in the order of 1 PeV or higher the tauon mean ranges will be tens or hundreds of meters. The decay follows an exponential distribution, so the distribution in ranges (r) will also be exponential with a mean range according to equation (6.2'):

$$f(r) = \frac{1}{R} \mathrm{e}^{-r/R} \ ; \qquad r \geq 0 \qquad (6.3)$$

As the tauon propagates through the detector medium it will loose energy, and one might ask how this will influence the tauon range. To determine this one needs to consider the energy loss per unit length. Two types of losses must be considered, ionization losses – which are high at low energies, drop to a minimum and then increase *slowly* with energy – and radiation losses – which are essentially proportional to the tauon energy at high energies. At high tauon energies (E_τ) the losses per unit length may therefore be approximated by a linear equation

$$-\frac{\mathrm{d}E_\tau}{\mathrm{d}x} \approx a_\tau + b_\tau \cdot E_\tau \qquad (6.4)$$

where a_τ is due to ionization losses and b_τ is due to radiation losses. Both a_τ and b_τ are slowly varying functions with energy, but according to [50] the asymptotic values for these functions at high energies are

$$\begin{cases} a_\tau \approx 0.2 \cdot \dfrac{\rho_{\text{ice}}}{\rho_{\text{water}}} \ \ \text{GeV} \cdot \text{m}^{-1} \\ b_\tau \approx 1.78 \cdot 10^{-6} \cdot \dfrac{\rho_{\text{ice}}}{\rho_{\text{water}}} \ \ \text{m}^{-1} \end{cases} \tag{6.5}$$

Assuming the approximate value $\rho_{\text{ice}} / \rho_{\text{water}} \approx 0.92$ for the relative density of ice at ~1 atm and temperatures close to 0 °C, one gets the result,

$$\begin{cases} a_\tau \approx 0.2 \ \ \text{GeV} \cdot \text{m}^{-1} \\ b_\tau \approx 1.6 \cdot 10^{-6} \ \ \text{m}^{-1} \end{cases} \tag{6.5'}$$

For a tauon with energy 1 PeV the mean range is ~50 m, and according to equations (6.4) and (6.5') it will loose ~2 GeV/m. This implies that only ~0.01% of its initial energy will be lost. For a 10 PeV tauon ~0.1% of the initial energy will be lost. The influence on the tauon range may therefore be neglected at these energies.

It is interesting to make a comparison with the muon energy losses. According to [50] the energy loss per unit length is roughly proportional to the inverse of the mass squared for the propagating particle. For a muon (μ)

$$-\frac{\text{d}E_\mu}{\text{d}x} \approx a_\mu + b_\mu \cdot E_\mu \quad , \tag{6.6}$$

where (for ice)

$$\begin{cases} a_\mu \approx a_\tau \approx 0.2 \ \ \text{GeV} \cdot \text{m}^{-1} \\ b_\mu \approx 219 \cdot b_\tau \approx 3.6 \cdot 10^{-4} \ \ \text{m}^{-1} \end{cases} . \tag{6.7}$$

A 1 PeV muon will thus loose almost 200 times more energy per unit length compared with a tauon of the same energy.

6.1.4 The tauon decay

The tauon decay is described by

$$\tau \rightarrow \nu_\tau + \text{"}anything\text{"} \ ,$$

where "*anything*" stands for either hadrons — probability ~65% — or leptons — $e + \bar{\nu}_e$: probability ~18% or $\mu + \bar{\nu}_\mu$: probability ~17% — [18]. If the decay follows either the hadronic channel or the leptonic channel to an electron and an electron neutrino, there will be a second "bang" completing the double-bang signature (two separate cascades). If the decay follows the leptonic channel to a muon and a muon neutrino, there will *not* be a second bang. Instead the emerging muon will continue the tauon track (possibly with small change in direction), emitting Čerenkov radiation.

6.2 Detection criteria

In chapter 9 an attempt is made to estimate the expected double bang event rates. For this purpose it is necessary to characterize the limitations of the detector. Following the discussion in [7] regarding the energy threshold for the detection of double bang events it is suggested that at least three detection criteria must be fulfilled:

1) For the double bang events to be detected it is essential that all three parts of the signature (the two cascades and the connecting tauon track) are sampled. It is reasonable to believe that this can only be done if the event is completely *contained* within the detector.
2) To be able to distinguish the two cascades from each other they must be sufficiently well separated. This *minimum separation* (r_{min}) will depend on the density and distribution of optical modules within the detector.
3) For a cascade to be recognized as such it must be very bright. Both cascades of a double bang event must therefore individually produce photons in numbers corresponding to an electromagnetic cascade exceeding some *minimal energy* (E_{min}).

These criteria will be used in section chapter 9.3 to develop a parameterized model for the "effective volume" (V_{eff}) of a generic detector, and to determine the V_{eff} values for the AMANDA-II and IceCube detectors (using the detector simulation routines described in section 7.3).

Chapter 7

Simulation- and analysis tools

7.1 Overview

To be able to study the properties of double bang events — described in chapter 6 — a number of FORTRAN programs were developed:

- for "generating" neutrinos and simulating the subsequent reactions (gen_nutau),
- for identifying events with the "double bang signature" and extracting relevant event information (ana_db),
- for simulating the detector response (db_det), and
- for analyzing the correlation between tauon range and visible energy produced when the tauon decays (corr_RE and histo_RE).

The order in which to use these programs is illustrated in figure 7.1.

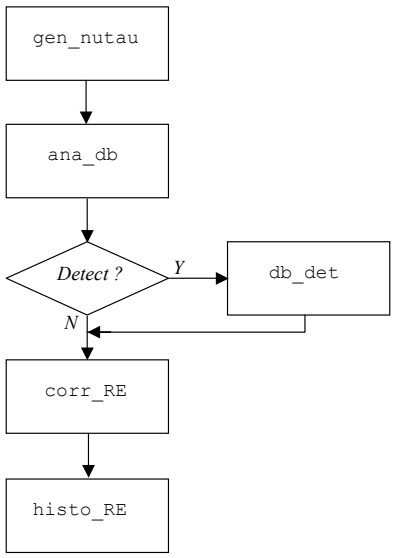

Figure 7.1 Illustration of the order in which to use the different simulation- and analysis tools for analyzing double bang events.

7.2 Event generator

To be able to study tau neutrino reactions with nucleons a generator program "gen_nutau" (written in FORTRAN 77) was developed. The FORTRAN routines in PYTHIA ver. 6.157 [51] were used for simulation of all primary particle reactions and for the particle production associated with tauon decay.

The program generates tau neutrinos with their momentum directed along the positive *z*-axis and with energies picked from a power-law spectrum specified by the user by giving the spectral index α according to equation 2.3. (Typical value: $\alpha = 2$. See section 2.2.3.) These neutrinos are made to react with either a proton or a neutron picked at random for each event. The probabilities for the two nucleon-types are preset to reflect the nucleon content of water. Thus, proton targets are selected with a probability of $10/18 \approx 56\%$, and neutron targets with $8/18 \approx 44\%$.

For each event only the particle production occurring within a small sphere (1 mm radius) centered at the reaction vertex is simulated. Any neutrinos are then removed. The information available for all remaining particles is saved to file together with some additional parameters like the energy of the parent neutrino and the inelasticity in the reaction. If a tauon has been produced PYTHIA computes the position of its decay. For tauons likely to reach distances consistent with a detectable double bang signature – as described in section 6.2 – energy losses for the propagation through the detector medium are considered negligible compared with the initial tauon energy (see section 6.1.3). Therefore *no* corrections are made either to the position where the tauon is made to decay or to the final energy of the tauon. After simulating the tauon decay (using the PYTHIA routines) all appearing neutrinos are removed, and the information about the remaining particles is saved to file.

During the investigations of the properties of double bang events it became clear that gen_nutau was not able to reproduce the expected cross sections – according to [22] – for neutrino-nucleon reactions. It turned out that the observed discrepancy was due to a combination of two different problems.

The first problem was that an incorrect method was used in gen_nutau for initiating and calling the PYTHIA routines. This had the effect of increasing the total cross section presented after each run by almost a factor two.

The second problem was an error in the PYTHIA routines themselves. After communicating with Joakim Edsjö (at Stockholm University) – who had also noticed an unexpected neutrino-nucleon cross section when using PYTHIA – and Torbjörn Sjöstrand (at Lund University) – who has the main responsibility for the development of PYTHIA – it was determined that the cross section for *neutral current reactions*, as presented by PYTHIA, was too small by a factor two (exactly[*]). The PYTHIA routines have since been corrected.

[*] The neutral current cross section calculated by PYTHIA was found to be a factor two too small *per reacting neutrino*. Thus, for generated neutrino-neutrino reactions, the neutral current cross section would have been a factor four too small.

Since the ratio between the charged current cross section according to `gen_nutau` and the expected ("standard") values according to [22] was roughly constant over *the whole energy range* of interest (0.1 PeV to 25 PeV) I decided *not* to redo the simulations. Instead the charged current cross sections were renormalized (essentially divided by two) in all calculations where the cross section matters (the event rate calculations). The cross section estimates thus obtained is correct within ~10% compared with "standard" values.

7.3 Detector simulation

A set of `FORTRAN` routines was developed to perform simple simulations of the detection of double-bang events. The main objective is to get a grasp of the impact the size and shape of a detector has on the efficiency for detecting these events. The routines were implemented in two different programs:

1) "`veff_mc`": This program generates fixed-energy tauon tracks (determines starting point and end point of each track) with directions selected at random according to an isotropic flux from above. The assumption of a zero flux from below is a reasonable first approximation since the earth is essentially opaque to ~1 PeV tau neutrinos (see section 2.4.2). The starting points of the tauon tracks are distributed at random, homogenously in a cube surrounding the detector. Three different geometries are supported by this program: cylindrical, cubic and spherical. The user also selects the dimensions of the detector and the volume (V_{gen}) of the surrounding cube where tauon tracks are initiated. An event is regarded as "detected" if the tauon track is fully contained within the detector volume and if its length exceeds a minimum value (r_{min}), which is set by the user. For N_{gen} generated events and N_{det} detected events the effective volume is calculated as $V_{\text{eff}}(E_\tau) = \frac{N_{\text{det}}}{N_{\text{gen}}} \cdot V_{\text{gen}}$, for tauons with initial energy E_τ.

2) "`db_det`": This program reads double bang events from a file (events first generated by `gen_nutau` and then processed by the analysis program "`ana_db`"), assigns a direction and a starting point to each tauon track, and then determines if the event fulfills three detection criteria: fully contained tauon track, length of tauon track exceeding a minimum value, and both cascades exceeding a minimum energy. As in `veff_mc`, directions are picked from an isotropic distribution from above and starting points are selected from a homogenous distribution within a cube surrounding the detector. The user selects the geometry and dimensions of the detector, the minimum separation and the volume in which the tauon production-points are distributed. The minimum-energy criterion for cascade energies is set to 1 TeV ("visible" energy – see sections 8.3.1 and 8.3.2). The program produces an output file containing those events that passed the detection criteria.

7.4 Analysis programs

Three different FORTRAN programs were developed for the purpose of analyzing double bang events generated by gen_nutau.

1) "ana_db": This program is designed for reading an input file generated by the program gen_nutau, identifying the double bang events and extracting information about these events. The information is written to a number of output files. One of these files contains the identified double bang events. Each event is described by a small number of parameters, including neutrino energy, tauon energy, tauon range and visible energies for the two cascades. This file is intended for further processing (e.g. by db_det) and analysis.

2) "corr_RE": This program is designed for reading an input file produced by ana_db (optionally post processed by db_det) and – for each double bang event – extracting the tauon range (R) and the visible energy for the second cascade (E). This information is used for calculating the correlation coefficient between these parameters etc., but in addition an output file is produced containing the (R,E) information for all events. This file is intended for a more detailed analysis of the correlation between the two event parameters.

3) "histo_RE": This program is designed for reading an (R,E) file produced by the program corr_RE, calculating an estimate for the visible energy (E_R) based on the observed tauon range (R) and comparing it to the observed visible energy (E) of the second cascade. The user has the opportunity to introduce different combinations of "measurement errors" (stochastic or systematic) for both the tauon range and/or the visible energy. The purpose for doing so is to be able to evaluate the effects of "measurement" on the correspondence between the E_R and E.

Chapter 8

Intrinsic properties of double bang events

8.1 Motivation

In chapter 10, a method for calibration of neutrino telescopes using double bang events is described. This method relies on knowing the relation between the tauon range (which has a mean value proportional to the tauon energy) and the visible energy at the tauon decay vertex.

In this chapter I present a Monte Carlo study aiming at finding the intrinsic properties of double bang events. The results may be used for evaluating the probability for any allowed "appearance" – regarding visible cascade "sizes" (energies) and cascade separation – of a double bang event, given the neutrino energy.

8.2 Simulations

Tau neutrinos were generated and made to react with nucleons in water/ice using the `PYTHIA` based software described in section 7.1. Double bang events were then extracted and analyzed.

Mono-energetic neutrino "beams" were generated for three different energies: $E_\nu = 0.25$ PeV, 2.5 PeV and 25 PeV. These selections sample an interval that essentially covers the energy region of interest for observing double bang events in 1 km^3 detectors like IceCube. For each energy, a total of 10000 neutrinos were generated.

The MC simulations resulted in files containing information about the particles produced in the reactions. Cascades may have both an electromagnetic and a hadronic component, but since the most important property is the expected number of photons produced, a "visible energy" value (E_{vis}) is calculated for each cascade. This value is obtained by adding the energies of the cascade initiators, weighting the electromagnetic component with 1.00 and the hadronic component with 0.80 to reflect the expected photon yield (see sections 5.1.2 and 5.1.3). In effect, the composite cascades are replaced by simple electromagnetic ones.

8.3 Results

8.3.1 Visible energy — first cascade

At the first vertex the tau neutrino interacts with a nucleon. From the text in section 6.1.2 and equation (6.1a) one deduces that the available energy is

$$E_1 = y \cdot E_\nu \tag{8.1}$$

where E_ν is the energy of the tau neutrino. The fraction of the available energy that is *visible* is denoted ε_1. In the MC simulations this number is obtained for each event as

$$\varepsilon_1 = \frac{E_{1\text{vis}}}{E_1} = \frac{1.00 \cdot E_1^{\text{em}} + 0.80 \cdot E_1^{\text{had}}}{E_1} \ , \tag{8.2}$$

where E_1^{em} is the amount of energy carried by initiators for electromagnetic cascades, and E_1^{had} is the amount of energy carried by initiators for hadronic cascades.

The ε_1-distributions are presented in figure 8.1. Since no neutrinos are produced all available energy goes into cascade initiators, and consequently at least 80% of the energy will be visible. For the ε_1-distributions there is no observable dependence on the neutrino energy! Mean values for the three different neutrino energies are presented in table 8.1.

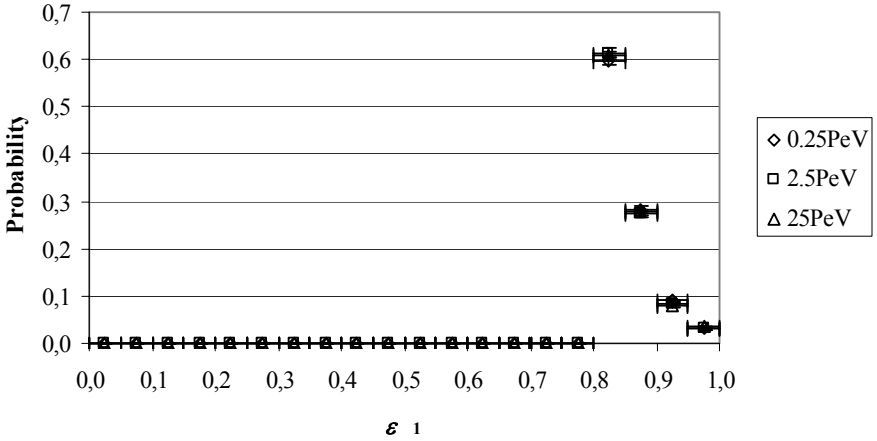

Figure 8.1 ε_1 is the fraction of available energy at the first vertex that will appear as visible energy (number of photons ∝ visible energy).

8.3.2 Visible energy — second cascade

At the second vertex the tauon produced in the charged current neutrino-nucleon reaction decays. According to section 6.1.3 a 1 PeV tauon has a mean range of ~50 m, and as it propagates it will radiate ~2 GeV/m. This suggests that only ~0.01% of the initial tauon energy will be radiated before decay. (A 10 PeV tauon would loose ~0.1% of its initial energy.) Neglecting the energy radiated by the tauon, the available energy at the second vertex according to equation (6.1a) is

$$E_2 \approx E_\tau = (1-y)\cdot E_\nu \quad , \tag{8.3}$$

where E_τ is the energy of the tauon *before* it starts to propagate through the ice.

As in the case of the first vertex the fraction of the available energy that is visible is denoted ε_2. In the MC simulations this is obtained for each event as

$$\varepsilon_2 = \frac{E_{2\text{vis}}}{E_2} = \frac{1.00\cdot E_2^{\text{em}} + 0.80\cdot E_2^{\text{had}}}{E_2} \quad , \tag{8.4}$$

where E_2^{em} is the amount of energy carried by initiators for electromagnetic cascades, and E_2^{had} is the amount of energy carried by initiators for hadronic cascades.

The ε_2-distributions are presented in figure 8.2. Here neutrinos *are* produced, and more energy will "disappear" without producing photons. As expected, for the ε_2-distributions, there is no observable dependence on the neutrino energy. Mean values for the three different neutrino energies are presented in table 8.1.

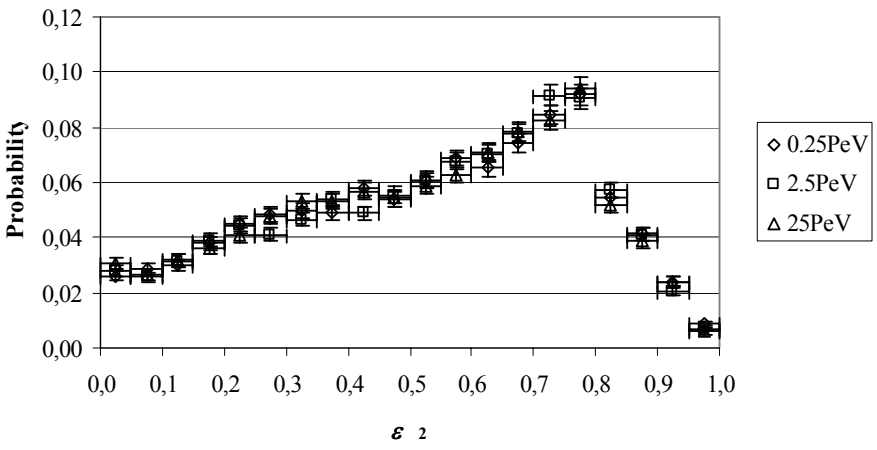

Figure 8.2 ε_2 is the fraction of available energy at the second vertex that will appear as visible energy (number of photons ∝ visible energy).

8.3.3 Inelasticity

The inelasticity (y) of the neutrino-nucleon reaction determines the ratio of available energy for the two cascades. Its distribution was extracted from the MC simulations, and it shows a gentle energy dependence in the studied energy region [0.25 PeV ; 25 PeV]. The distributions are presented in figure 8.3. It is apparent that the main effect of increasing the neutrino energy is a larger fraction of small-y events. A comprehensive description of this behavior may be found in [23]. Mean values for the three different energies are presented in table 8.1. Note however that the inelasticity distributions depend on the parton distributions of the target nucleons. These parton distributions are not known from first principles, but are determined from experiment. For the reactions studied here, the parton distributions are described by modern parameterizations (CTEQ-5M – as implemented in the `PYTHIA` routines).

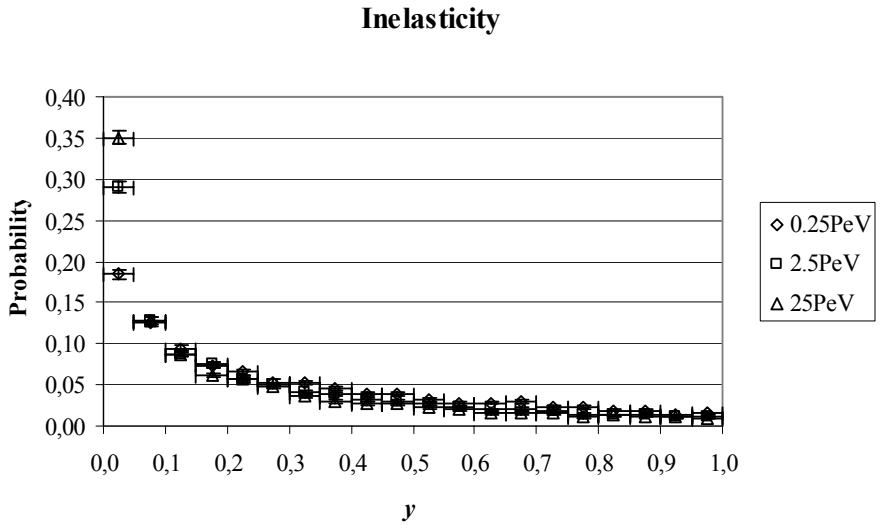

Figure 8.3 The inelasticity (y) is the fraction of the incident-neutrino energy that will be transferred to the struck quark.

E_ν [PeV]	$\langle y \rangle$	$\langle \varepsilon_1 \rangle$	$\langle \varepsilon_2 \rangle$
0.25	0.30	0.85	0.53
2.5	0.24	0.85	0.53
25	0.21	0.85	0.52

Table 8.1 Mean values for the inelasticity parameter y, for the visible-energy fraction ε_1 (first cascade) and for ε_2 (second cascade). These values are based on a total of 10000 simulated neutrino-nucleon reactions for each neutrino energy.

8.3.4 Tauon range

Given the tauon energy and neglecting energy losses along the "tauon track" the expected tauon range is given by equation (6.2'). For completeness – and as a simple cross-check of the routines – the tauon mean ranges extracted from the MC simulations were compared with the expected mean ranges given the extracted mean tauon energies. As expected, the two different mean-range estimations are found to be consistent with each other (see table 8.2).

E_ν [PeV]	$\langle R_\tau \rangle$ [m]	49m·$\langle E_\tau \rangle$/1PeV
0.25	8.481±0.081	8.581±0.043
2.5	92.5±1.5	92.95±0.34
25	968.6±9.7	963.7±5.8

Table 8.2 Comparison between mean tauon range and a mean-range estimate based on the mean tauon energy. These values (with statistical errors) are based on a total of 10000 simulated neutrino-nucleon reactions for each selection of neutrino energy. The two mean-range estimations are found to be consistent with each other.

Chapter 9

Anticipated event rates

9.1 Motivation

The potential power of the energy calibration method described in chapter 10, depends on the expected annual number of detected double bang events.

In this chapter I present estimations of the double bang event rates in AMANDA-II and in IceCube for a typical neutrino spectrum. This is done in three steps:

1) An expression for transforming a neutrino flux to the corresponding double bang production rate is presented. This expression is then evaluated by performing Monte Carlo simulations of a large number of neutrino reactions.
2) A simple analytical model is presented describing the effective detector volume for double bang events. A Monte Carlo program is then used to simulate the detector responses and estimate the free parameters of this model with respect to AMANDA-II and IceCube.
3) The anticipated event rates for these two detectors are calculated using the production rate and effective volume expressions obtained in steps 1 and 2.

9.2 Double bang production rate

9.2.1 Model

The flux of cosmic tau neutrinos is often parameterized as

$$\Phi_\nu(E_\nu) = \Phi_{\nu 1} \cdot \left(\frac{E_\nu}{1\,\mathrm{PeV}} \right)^{-a} \ \mathrm{m}^{-2} \cdot \mathrm{yr}^{-1} \cdot \mathrm{PeV}^{-1} \cdot \mathrm{sr}^{-1} \ , \qquad (9.1)$$

[15] where proposed values on the constant $\Phi_{\nu 1}$ may be obtained from section 2.5 for fluxes with $a = 2$. (A power-law spectrum with a spectral index ~2 is typical for sources where particles have been accelerated in supersonic shocks [16].)

The corresponding double bang production rate is

$$n_{\mathrm{db}}(E_\tau) = \varepsilon \cdot \rho \cdot N_{\mathrm{A}} \cdot \int \Phi_\nu(E_\nu) \cdot \frac{\mathrm{d}\sigma_{\mathrm{CC}}(E_\tau; E_\nu)}{\mathrm{d}E_\tau} \mathrm{d}E_\nu \ \ \mathrm{m}^{-3} \cdot \mathrm{yr}^{-1} \cdot \mathrm{PeV}^{-1} \cdot \mathrm{sr}^{-1} \ . \tag{9.2}$$

In this expression an approximate value $\rho \approx 0.92 \cdot 10^3$ kg/m^3 (at -4°C, 1 atm) was used for the density of ice; $N_{\mathrm{A}} = 6.022 \cdot 10^{26}$ kg^{-1} is the Avogadro constant; $\varepsilon \approx 0.83$ is the fraction of tauon decays that result in a cascade[*]; $\mathrm{d}\sigma_{\mathrm{CC}}(E_\tau; E_\nu)/\mathrm{d}E_\tau$ is the differential CC cross section for a neutrino of energy E_ν to convert to a tauon of energy E_τ.

9.2.2 Simulations

To evaluate equation (9.2), a Monte-Carlo simulation of tau neutrino reactions was performed using the generator `gen_nutau` described in section 7.2. The total simulated energy range was $0.1\ \mathrm{PeV} < E_\nu < 25\ \mathrm{PeV}$. In this range the reaction cross-section is not constant and this must, for technical reasons[**], be taken into account already in the set-up of the simulation.

As a first step, the energy dependence of the cross-section must therefore be described. In [22] the CETEQ4-DIS cross-sections are tabulated. I used these values to perform a least-square fit to the following parameterization:

$$\sigma_{\mathrm{tot}}(E_\nu) = \sigma_1 \cdot \left(\frac{E_\nu}{1\ \mathrm{PeV}} \right)^b \ \mathrm{m}^2 \quad ; \qquad 0.1\ \mathrm{PeV} < E_\nu < 100\ \mathrm{PeV} \tag{9.3}$$

The model parameters thus obtained are: $\sigma_1 = 8.77 \cdot 10^{-38}$ m^2 and $b = 0.435$. For $0.25\ \mathrm{PeV} < E_\nu < 100\ \mathrm{PeV}$ this expression does not differ from any of the tabulated values with more than 6%, and at $E_\nu = 0.1\ \mathrm{PeV}$ the difference is 15%. For this parameterization the total number of neutrino reactions may be expressed as

$$n_{\mathrm{tot}} = \rho \cdot N_A \cdot \sigma_1 \cdot \Phi_{\nu 1} \cdot \int \left(\frac{E_\nu}{1\ \mathrm{PeV}} \right)^{b-a} \mathrm{d}E_\nu \qquad \mathrm{m}^{-3} \cdot \mathrm{yr}^{-1} \cdot \mathrm{sr}^{-1} \ . \tag{9.4}$$

Thus, in the simulation tau neutrino energies are picked from the distribution

$$f(E_\nu) = \left(\frac{1-\alpha}{E_2^{1-\alpha} - E_1^{1-\alpha}} \right) \cdot E_\nu^{-\alpha} \ \mathrm{PeV}^{-1} \ , \tag{9.5}$$

where $E_1 = 0.1$ PeV, $E_2 = 25$ PeV and $\alpha = a\text{-}b = 1.57$.

[*] The remaining 17% of the tauon decays are given by $\tau \to \mu + \overline{\nu_\mu} + \nu_\tau$.

[**] Neutrino energies are picked from a distribution, and are *forced* to interact with a nucleon. To account for the fact that the probability for interaction is different at different neutrino energies, the shape of the initial neutrino spectrum must be modified.

The number of tau neutrino reactions generated was $K = 10000$, and the event files produced by the generator were analyzed using the program `ana_db` described in section 7.4. As a result a histogram was produced, representing the tauon-energy distribution for those events where the tauon did *not* decay to a muon (and two neutrinos): $k(E_\tau)$ denotes the number of events in a bin centered at E_τ, with the bin widths set to $\Delta E = 0.5$ PeV. The histogram was used to evaluate the tauon production rate according to the following expression:

$$n_{\mathrm{db}}(E_\tau) = \frac{k(E_\tau)}{K \cdot \Delta E} \cdot n_{\mathrm{tot}} \ \ \mathrm{m}^{-3} \cdot \mathrm{yr}^{-1} \cdot \mathrm{PeV}^{-1} \cdot \mathrm{sr}^{-1} \ , \tag{9.6}$$

where in this case $n_{\mathrm{tot}} = 3.03 \cdot 10^{-7} \cdot \Phi_{\nu 1} \ \ \mathrm{m}^{-3} \cdot \mathrm{yr}^{-1} \cdot \mathrm{sr}^{-1}$ according to (9.4).

9.2.3 Result

The double-bang production rate for a flux normalized to $\Phi_{\nu 1} = 1 \ \mathrm{m}^{-2} \cdot \mathrm{yr}^{-1} \cdot \mathrm{PeV}^{-1} \cdot \mathrm{sr}^{-1}$, is presented in figure 9.1. The bin width is $\Delta E = 0.5$ PeV. Also included in the plot is a least-square fit to the parameterization

$$n_{\mathrm{db}}(E_\tau) = n_1 \cdot \left(\frac{E_\tau}{1 \ \mathrm{PeV}} \right)^{-\alpha'} \ \ \mathrm{m}^{-3} \cdot \mathrm{yr}^{-1} \cdot \mathrm{PeV}^{-1} \cdot \mathrm{sr}^{-1} \ . \tag{9.7}$$

This fit was made for $1 \ \mathrm{PeV} < E_\tau < 24 \ \mathrm{PeV}$ - i.e. excluding two bins in each end of the spectrum – a restriction introduced to avoid the cut-off region, due to the limitation in the simulated neutrino-energy interval. The production rate at 1 PeV and spectral index was found to be $n_1 = 4.24 \cdot 10^{-8} \ \ \mathrm{m}^{-3} \cdot \mathrm{yr}^{-1} \cdot \mathrm{PeV}^{-1} \cdot \mathrm{sr}^{-1}$ and $\alpha' = 1.64$ respectively. This expression will be used in chapter 10 for the analysis of the relation between tauon ranges and tauon energies.

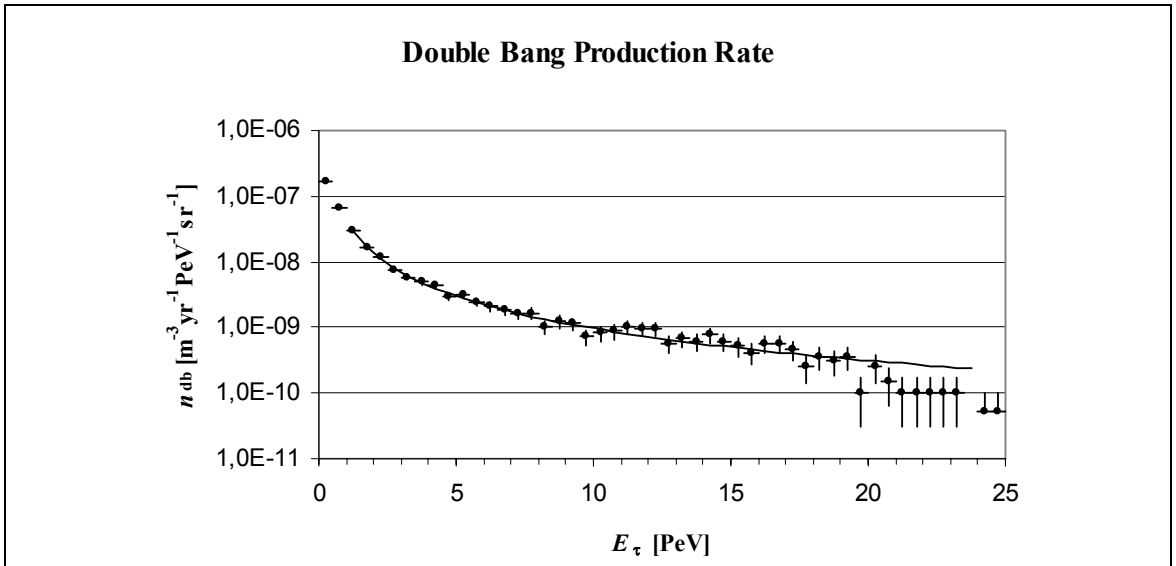

Figure 9.1 The anticipated double-bang production rate assuming a generic $\Phi_{\nu 1} \cdot (E_\nu / 1 \ \mathrm{PeV})^{-2}$ tau neutrino flux, with $\Phi_{\nu 1} = 1 \ \mathrm{m}^{-2} \cdot \mathrm{yr}^{-1} \cdot \mathrm{PeV}^{-1} \cdot \mathrm{sr}^{-1}$. The dots are the simulated values and the line represents a least-square fit to $n_{\mathrm{db}}(E_\tau) = n_1 \cdot (E_\tau / 1 \ \mathrm{PeV})^{-1.64}$, for $1 \ \mathrm{PeV} < E_\tau < 24$ PeV. The differential event rate at $E_\tau = 1$ PeV was found to be $n_1 = 4.24 \cdot 10^{-8} \ \mathrm{m}^{-3} \mathrm{yr}^{-1} \mathrm{PeV}^{-1} \mathrm{sr}^{-1}$.

9.3 Effective volume

9.3.1 Model

A double bang event is characterized by the amount of photons produced in the two cascades, and by the cascade separation (tauon range). As was suggested in section 6.2, to be considered as "detected" an event should be fully contained within the detector volume, the separation should exceed a minimum value ($r_{\min}$) and both cascades should be energetic enough to be detected.

To estimate the expected detection rate (n_{det}), the production rate per unit volume ($n_{\text{gen}}/V_{\text{gen}}$) is multiplied with the effective detector volume (V_{eff}). Given that essentially all cascades are energetic enough for detection – and this is assumed to be the case from here on – the effective volume will only depend on the tauon energy:

$$V_{\text{eff}}(E_\tau) = \frac{n_{\text{det}}(E_\tau)}{n_{\text{gen}}(E_\tau)} \cdot V_{\text{gen}} \tag{9.8}$$

A phenomenological model for V_{eff} may be obtained by considering a simplified situation: Consider a tau neutrino flux directed perpendicular to a flat detector with an exposed area A_{eff} and a thickness L. A tauon track of length r will only be fully contained if the tauon is produced no "deeper" than $(L - r)$ measured from the surface facing the neutrino source. This limits the detection volume for such tracks to $A_{\text{eff}} \times (L - r)$. By weighting this volume with the range probability density according to equation (6.3), and integrating over the allowed range interval the final expression is found:

$$V_{\text{eff}}(E_\tau) = A_{\text{eff}} \int_{r_{\min}}^{L} (L - r) \cdot \frac{e^{-r/R}}{R} \cdot \mathrm{d}r = A_{\text{eff}} \left[(L - r_{\min} - R) \cdot e^{-r_{\min}/R} + R \cdot e^{-L/R} \right], \tag{9.9}$$

where $R = R(E_\tau)$ is the mean range according to equation (6.2').

Since $r_{\min}$ is assumed to be a *known* limitation of the detection process, equation (9.9) suggests that the (energy dependent) effective volume is defined only by the exposed area (A_{eff}) and the thickness (L) of the detector.

9.3.2 Simulations

A series of Monte Carlo simulations were performed using the program `veff_mc` described in section 7.3. The purpose for these simulations was to meet two objectives:

1) to verify that the equation (9.9) is valid when considering the three-dimensional nature of the detector and of the tauon production.
2) to determine the model parameters A_{eff} and L for both AMANDA-II and IceCube.

In the simulations tauon energies were selected in steps of 0.5 PeV in the interval $0.5\ \text{PeV} \le E_\tau \le 15\ \text{PeV}$. For each energy-selection the simulation continued until 10000 events had been detected, detection criteria being: fully contained tauon track, and cascade separation exceeding $r_{\min}$. Tauon tracks were generated in a volume (V_{gen}) surrounding the detector, with directions of origin picked from an isotropic distribution from the upper hemisphere.

For AMANDA-II the following settings were used:

- Detector geometry and dimensions: cylinder; height 500 m, radius 100 m
- Minimum cascade separations: $r_{\min} = 100$ m or 250 m
- Generation volume: $V_{\text{gen}} = 1.6 \cdot 10^8\ \text{m}^3$ (~10× the physical detector volume)

For IceCube the following settings were used:

- Detector geometry and dimensions: cylinder; height 950 m, radius 550 m
- Minimum cascade separations: $r_{\min} = 100$ m or 250 m
- Generation volume: $V_{\text{gen}} = 9.0 \cdot 10^9\ \text{m}^3$ (~10× the physical detector volume)

For each simulation the effective volume was calculated according to equation (9.8), with n_{gen} equal to the number of generated events necessary to obtain the required number of detected events: $n_{\text{det}} = 10000$.

9.3.3 Results

For each of the two simulated detectors – with the relevant detector parameters given in section 9.3.2 – the model parameters (A_{eff} and L) were obtained by performing a least square fit of expression (9.9) to the simulation results (see figure 9.2). The results for the two detectors are:

- AMANDA-II ($r_{\min} = 100$ m): $A_{\text{eff}} = 3.87 \cdot 10^4\ \text{m}^2$. $L = 261$ m.
- AMANDA-II ($r_{\min} = 250$ m): $A_{\text{eff}} = 3.83 \cdot 10^3\ \text{m}^2$. $L = 421$ m.
- IceCube ($r_{\min} = 100$ m): $A_{\text{eff}} = 8.96 \cdot 10^5\ \text{m}^2$. $L = 928$ m.
- IceCube ($r_{\min} = 250$ m): $A_{\text{eff}} = 8.08 \cdot 10^5\ \text{m}^2$. $L = 962$ m.

From the plots in figure 9.2 it is clear that the effective volume for these two detectors is well described by equation (9.9). Apparently the essential properties of these detectors are preserved in the mathematical model, despite the simplifications made in deriving it. The geometry (cylindrical, cubic etc) and size of a detector in combination with the value of the minimum cascade separation $r_{\min}$ determines both the "shape" of the energy dependent effective volume and the normalization factor. For a given $r_{\min}$ value the *shape* may be recreated in the effective-volume function (9.9) by variation of the effective length parameter, L. The *normalization factor* may be recreated by variation of the effective area parameter, A_{eff}.

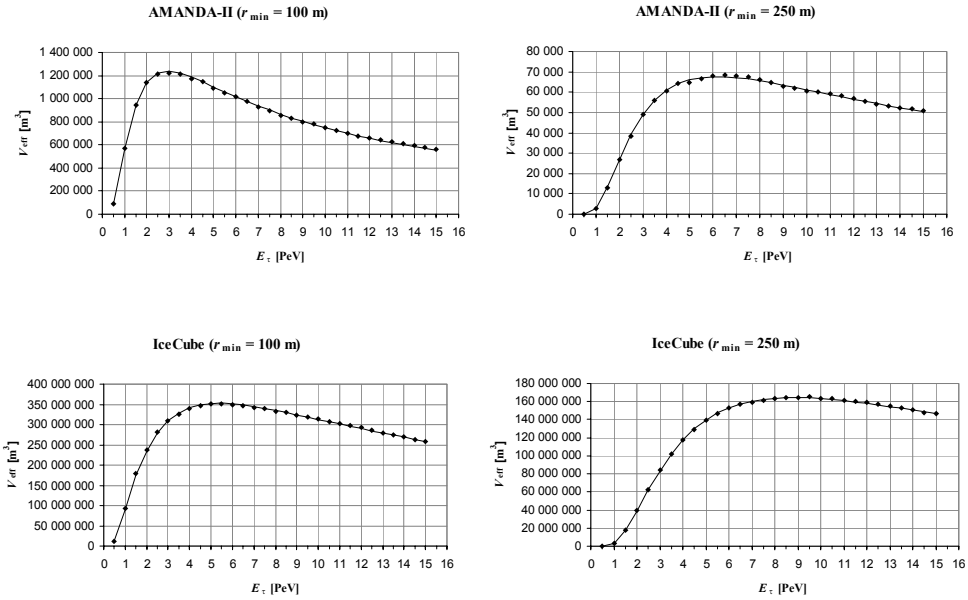

Figure 9.2 Effective detector volumes for double bang events in AMANDA-II and in IceCube. Two different values for the minimum cascade separation ($r_{\min}$) are considered. Diamonds represent the simulation results. Lines represent the least square fits of the proposed two-parameter (A_{eff} and L) model.

9.4 Event rate calculations

The anticipated double bang event rates (N_{db}) can now be calculated by multiplying the tauon production rate obtained in section 9.2 with the effective volumes obtained in section 9.3, and integrating over the relevant tauon energy range. In principle one should also integrate over all solid angles, but this integration was performed numerically when determining the model parameters in the expression for the effective volume. Therefore the solid angle, $\Omega_\nu = 2\pi$ steradians for the isotropic neutrino flux from the upper hemisphere, is regarded as a constant normalization factor in this case:

$$N_{\text{db}} = \Omega_\nu \cdot \int n_{\text{db}}(E_\tau) \cdot V_{\text{eff}}(E_\tau) \cdot \mathrm{d}E_\tau \ \ \text{yr}^{-1} \tag{9.10}$$

When evaluating the event rate according to (9.10) equation (9.7) was used for the double bang production rate and equation (9.9) for the effective volume, and the selected energy range was $0.25 \text{ PeV} < E_\tau < 25 \text{ PeV}$. Different detector configurations are defined by selecting the appropriate values for A_{eff}, $r_{\min}$ and L, and different neutrino sources are defined by selecting the appropriate values for $\Phi_{\nu 1}$. The rates are presented in table 9.1 and cover all combinations of the four neutrino flux estimates introduced in section 2.5 and three different detector configurations - AMANDA-II, IceCube and a *generic* detector with the following characteristics:

$A_{\text{eff}} = 1\ \text{km}^2$
$r_{\text{min}} = 0.1$ km
$L = 1$ km

The configuration of the generic detector is identical to the one used in [25] for estimating the detection rate from gamma ray bursts. A direct comparison between estimates for the maximal GRB flux (Lorentz factor $\Gamma = 100$; labeled "GRB" in table 9.1), shows that the stated rate of 0.54 down going double-bang events per year is notably higher than the value presented here (0.15 yr^{-1}).

ν_τ source	AMANDA-II (r_{min}=100m)	AMANDA-II (r_{min}=250m)	IceCube (r_{min}=100m)	IceCube (r_{min}=250m)	"Generic" (r_{min}=100m)
"$\Phi_{\nu l}$=1"	*0.42 yr^{-1}*	*$1.3 \cdot 10^{-2}$ yr^{-1}*	*99 yr^{-1}*	*27 yr^{-1}*	*123 yr^{-1}*
GRB	$5.2 \cdot 10^{-4}$ yr^{-1}	$1.6 \cdot 10^{-5}$ yr^{-1}	0.12 yr^{-1}	$3.4 \cdot 10^{-2}$ yr^{-1}	0.15 yr^{-1}
WB limit	$1.0 \cdot 10^{-3}$ yr^{-1}	$3.3 \cdot 10^{-5}$ yr^{-1}	0.25 yr^{-1}	$6.7 \cdot 10^{-2}$ yr^{-1}	0.31 yr^{-1}
AGN-HC	0.19 yr^{-1}	$5.9 \cdot 10^{-3}$ yr^{-1}	45 yr^{-1}	12 yr^{-1}	55 yr^{-1}
AM-B10 limit	0.13 yr^{-1}	$4.0 \cdot 10^{-3}$ yr^{-1}	30 yr^{-1}	8.1 yr^{-1}	37 yr^{-1}

Table 9.1 Typical event rates for different neutrino sources and detector configurations. The "$\Phi_{\nu l}$=1" source does *not* correspond to any proposed flux. It is simply a flux normalized to $\Phi_{\nu l}=1\text{m}^{-2}\cdot\text{yr}^{-1}\cdot\text{PeV}^{-1}\cdot\text{sr}^{-1}$. "GRB" is the maximum GRB flux according to [25] assuming a mixing scenario where the tau neutrino flux equals half of the generated muon neutrino flux. "WB" is the Waxman-Bahcall upper limit [27] in the same mixing scenario. "AGN-HC" is the flux from the interior of "optically thick" AGNs (Hidden Core) according to [26] and assuming maximal mixing. "AM-B10 limit" is the upper limit (extrapolated) obtained by muon-neutrino observations with the AMANDA-B10 detector (1997 year data) [28] assuming "distant sources" and maximal two-flavor mixing (equal amounts of tau neutrinos and muon neutrinos).

9.5 Conclusions

In this chapter a method was presented for deriving the expected double bang event rates given the neutrino flux and the detector configuration (geometry, dimension and "threshold"). The rates were also evaluated for a few example fluxes and detector configurations.

One of the results from this evaluation is expression (9.7) for the double-bang energy distribution. This expression will be used in chapter 10 as part of the information needed to define a relation between the observed cascade separation and the "expected" visible energy from the corresponding tauon decay.

From the study of the example detectors a couple of observations can be made about the event rates. Given the minimum cascade separation r_{min} – essentially defining the energy threshold – the double bang event rate is *not* proportional to its volume, but increases *faster* with volume. The reason is that a larger detector will also be sensitive to events in a wider energy range. Another possible way of increasing the event rate is to try to resolve events with smaller values on r_{min}. This both lowers the threshold and increases the detection probability since short-track events will result from events over the whole energy range.

The rates presented in table 9.1 seem to indicate that the double bang event rate will be too small for calibration purposes in the AMANDA-II detector. One would have to reduce $r_{\min}$ to ~60 m to reach an event rate of 1 yr^{-1} at the AMANDA-B10 limit. In IceCube and other km-scale detectors the event rates will possibly be sufficient if the tau neutrino flux is not much smaller than what is allowed by the AMANDA-B10 limit. It may be noted that in order to reach an event rate of 1 yr^{-1} at the Waxman-Bahcall limit in a generic 1 km^3 detector one would have to reduce $r_{\min}$ to ~25 m.

Finally, using the concept of effective volume, it is possible to make a rough estimate of the signal-to-background ratio. In section 6.1.1 it was stated that the most serious background events will be muon neutrino CC events where the muon travels approximately 100 m before loosing most of its energy in a single bremsstrahlung reaction. According to [7] the fraction of muon neutrino CC events having a signature similar to this is expected to be of the order $P_{\mathrm{CC}\rightarrow\mathrm{fake}} = 3 \cdot 10^{-3}$.

The effective volume for double bang events with a cascade separation of 100 m is roughly $V_{100} = 1 \cdot 10^7$ m^3 for AMANDA-II and $V_{100} = 8 \cdot 10^8$ m^3 for IceCube. Assuming equal amounts of tau neutrinos and muon neutrinos (and similar CC cross-sections) the signal-to-noise ratio may be estimated by the following expression:

$$SN(E_\tau) = \frac{\varepsilon \cdot V_{\mathrm{eff}}(E_\tau)}{P_{\mathrm{CC}\rightarrow\mathrm{fake}} \cdot V_{100}} \ , \tag{9.11}$$

where $\varepsilon \approx 0.83$ is the fraction of tauon decays that result in a cascade.

For $r_{\min} = 100$ m the energy threshold is roughly $E_\tau \approx 2$ PeV (the tauon energy corresponding to a tauon range equal to the minimum separation $r_{\min}$). At this threshold $SN \approx 30$ for AMANDA-II and $SN \approx 80$ for IceCube. These SN values will improve if the threshold is lowered.

Chapter 10

Energy calibration

10.1 Motivation

One important objective in neutrino telescopy is to determine the neutrino energy. This is done in two steps: First the energy of the muon or cascade is determined. Then this energy is used to estimate the neutrino energy.

For *muon tracks at low energies* a method for energy calibration has been suggested [53] that uses muons that stop within the detector. The length of the track segment within the detector is related to the initial energy of the muon. This independent energy estimation can be compared with the reconstructed energy obtained by the standard algorithm.

In this chapter a similar calibration method for *cascades*, using double bang events, will be described. It relies on the fact that the mean range of the tauon is proportional to the tauon energy. A measurement of the cascade separation will thus provide an independent energy-estimation for the cascade energy at the decay vertex.

One potential application involving the detection of double bang events is to try to estimate the mean value of the inelasticity $< y >$ for UHE neutrino nucleon reactions, which could provide information about the small x behavior of the nucleon structure function [23]. The inelasticity in an event is given by $y = 1 - E_\tau / E_\nu$ according to equation (8.3). The tauon energy E_τ could be estimated from the reconstructed energy of the second cascade and the neutrino energy E_ν could be estimated from the reconstructed energies of both cascades. One important factor for the success of this type of study is of course an accurate energy reconstruction algorithm.

10.2 Method

10.2.1 Energy estimation

In this study the energy spectrum of the tau neutrino flux is assumed to be known, e.g. from detection and energy reconstruction of muon neutrinos. As an example, the calibration method will be evaluated for a typical tau neutrino flux, proportional to E_ν^{-2}.

In section 9.2.3 it was shown that the energy spectrum for the corresponding tauons will be more "flat" due to the increasing neutrino-nucleon cross section at increasing neutrino energies. Thus, in accordance with the result presented in section 9.2.3 the tauon flux is assumed to be proportional to $E_\tau^{-\alpha}$, where the spectral index $\alpha \approx 1.6$.

An expression may now be derived estimating the visible energy at the tauon decay vertex for a given cascade separation (tauon range). The tauon energy estimates are found by optimizing for smallest possible r.m.s. errors. (Note that other ways to define an estimate are possible, depending on the purpose of the study.) Given the tauon energy the visible energy at the tauon decay vertex is then estimated by a constant fraction of the tauon energy:

$$E_{vis} = <\varepsilon> \cdot E_\tau \ , \tag{10.1}$$

where $<\varepsilon>$ = 0.53 is the mean value of the probability distribution presented in section 8.3.2.

First the prior probability distribution for the tauon energy is defined as

$$f(E_\tau) = \frac{1-\alpha}{E_2^{1-\alpha} - E_1^{1-\alpha}} \cdot E_\tau^{-\alpha} \qquad ; \qquad E_1 < E_\tau < E_2 \ , \tag{10.2}$$

where the energy interval $E_1 < E_\tau < E_2$ should cover the sensitive region for the specific detector. The conditional probability distribution for the tauon range (r), given the tauon energy, is presented in equation (6.3):

$$f(r|E_\tau) = \frac{1}{R} \cdot e^{-r/R} \qquad ; \qquad R = \frac{E_\tau}{m_\tau c^2} \cdot c t_\tau = \underbrace{(49.03\ \mu\mathrm{m/GeV})}_{=C_1} \cdot E_\tau \tag{10.3}$$

From Bayes' theorem one can now obtain the conditional probability distribution for E_τ, given the tauon range:

$$f(E_\tau|r) = \frac{f(r|E_\tau) \cdot f(E_\tau)}{\int_{E_1}^{E_2} f(r|E_\tau) \cdot f(E_\tau) \cdot \mathrm{d}E} \propto f(r|E_\tau) \cdot f(E_\tau) \propto E_\tau^{-(\alpha+1)} \cdot e^{-r/C_1 E_\tau} \ . \tag{10.4}$$

In general it is now possible to use equation (10.4) to define a suitable energy estimate, depending on the purpose of the study. For example, since $f(E_\tau|r)$ has a maximum value, one may want to use this *most probable* value. Another possibility is to calculate the *mean* value. In the present study an energy estimate with a *narrow error distribution* is favorable. Thus, the *Least-Square* (LS) estimate of the tauon energy ($\widetilde{E}_\tau$) is selected, which is determined by minimizing

$$\chi^2(\widetilde{E}_\tau) = \int_{E_1}^{E_2} (E_\tau - \widetilde{E}_\tau)^2 \cdot f(r|E_\tau) \cdot f(E_\tau) \cdot \mathrm{d}E_\tau = \underbrace{\int_{E_1}^{E_2} E_\tau^2 \cdot f(r|E_\tau) \cdot f(E_\tau) \cdot \mathrm{d}E_\tau}_{=I_1} +$$

$$\underbrace{\widetilde{E}_\tau^2 \int_{E_1}^{E_2} f(r|E_\tau) \cdot f(E_\tau) \cdot \mathrm{d}E_\tau}_{=I_2} - 2\widetilde{E}_\tau \underbrace{\int_{E_1}^{E_2} E_\tau \cdot f(r|E_\tau) \cdot f(E_\tau) \cdot \mathrm{d}E_\tau}_{=I_3} \qquad (10.5)$$

$$0 = \frac{d\chi^2}{d\widetilde{E}_\tau} = 2\widetilde{E}_\tau I_2 - 2I_3 \qquad \Rightarrow$$

$$\Rightarrow \qquad \widetilde{E}_\tau(r) = \frac{I_3}{I_2} = \frac{\int_{E_1}^{E_2} E_\tau^{-\alpha} \cdot e^{-r/C_1 E_\tau} \mathrm{d}E_\tau}{\int_{E_1}^{E_2} E_\tau^{-(\alpha+1)} \cdot e^{-r/C_1 E_\tau} \mathrm{d}E_\tau} \qquad (10.6)$$

The integrals on the right side of equation 10.6 were evaluated numerically for different tauon ranges, $100\ \mathrm{m} \le r \le 1000\ \mathrm{m}$. The selected limits of integration were $E_1 = 0.1$ PeV and $E_2 = 100$ PeV, thus covering the sensitive region for the telescopes studied in this thesis. The results were used to calculate $\widetilde{E}_\tau(r)$ for the selected values on r, and a second order polynomial fit (requiring $\widetilde{E}_\tau(0) = 0$) was determined:

$$\widetilde{E}_\tau(r) = ar + br^2 \ , \qquad (10.7)$$

with the parameter values $a = 0.0281$ PeV/m and $b = -7.33 \cdot 10^{-6}$ PeV/m^2.

Finally, these tauon energies were converted into visible-energy estimates (E_R) using the average visible-energy fraction according to equation (10.1)*:

$$E_R(r) = <\varepsilon> \cdot \widetilde{E}_\tau(r) = <\varepsilon> \cdot (ar + br^2) \qquad (10.8)$$

The final result is presented in figure 10.1. In this plot one may note that since the distribution seems to be denser below the line representing the LS estimates, the corresponding *mean value* estimates would probably point at lower energies.

* This approach is a simplification that disregards the prior distribution of the visible energy.

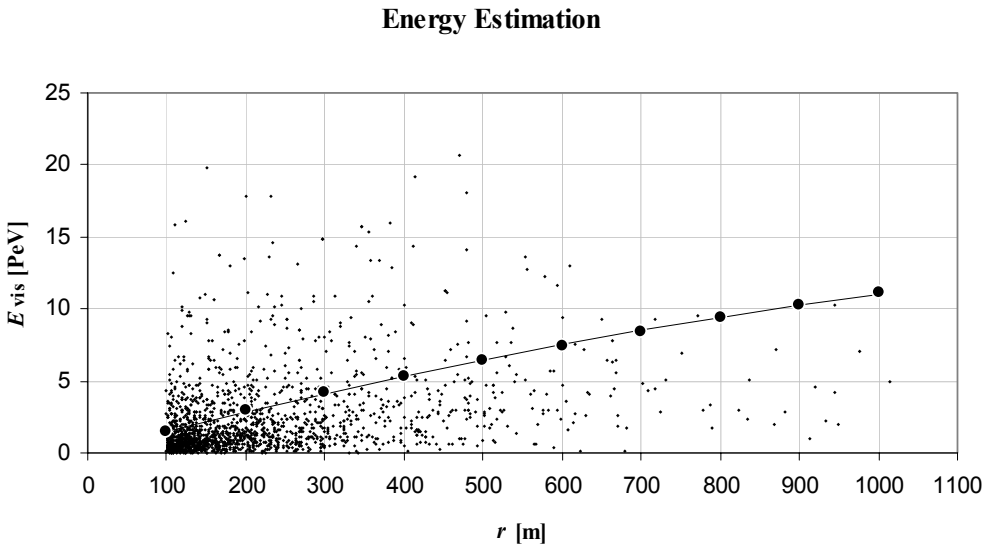

Figure 10.1. The visible energy (E_{vis}) at the tauon decay vertex may be estimated in double-bang events from the separation between the two cascades (the tauon range, r). A least-square estimate was determined and parameterized, assuming a neutrino flux $\Phi_\nu \propto E_\nu^{-2}$. The result is: $E_R = \langle\varepsilon\rangle \cdot (a \cdot r + b \cdot r^2)$, where $\langle\varepsilon\rangle = 0.53$, $a = 0.0281$ PeV/m and $b = -7.33 \cdot 10^{-6}$ PeV/m^2. Also shown is a sample of simulated (r,E_{vis}) points representing detected double-bang events in IceCube, with $r > 100$ m.

10.2.2 Simulation

Five simulation runs were made using the Monte Carlo program `gen_nutau`. In each simulation 50000 neutrino-nucleon reactions were generated. The double bang information was extracted using the program `ana_db`. These double bang events were then processed by the program `dbdet` simulating the detection process in IceCube. This program assigns a position for the first cascade of each event. These positions are selected from a homogenous distribution inside a cubic generation volume surrounding the detector volume. A direction-of-origin is selected from an isotropic distribution from the upper hemisphere, and the position of the second vertex is determined. An event is then labeled "detected" if three detection criteria are fulfilled:

- Both vertices are found within the detector volume.
- The separation exceeds a minimum separation $r_{min} = 100$ m.
- Both cascades have visible energies exceeding 1 TeV.

Since the generation volume must be much larger than the detector volume to reduce the edge effects only a fraction of the events will be detected. With a generation volume ten times as large as the detector the `dbdet` program was allowed to "reuse" the generated double-bang events ~10 times. Each event is then expected to have its first cascade within the detector volume once (on average).

10.2.3 Analysis

After applying the detection procedure 5000 events remained. (1000 events were produced from each 50000-event simulation.) These double-bang events were analyzed using the program `histo_RE`, which produces a histogram for $\log_{10}(E_{vis}/E_R)$. The program offers the option of introducing "measurement errors", and this option was invoked to mimic the expected uncertainties in both r (Gaussian error distribution, $\sigma = 5$ m) and $\log_{10}(E_{vis}/1\text{PeV})$ (Gaussian error distribution, $\sigma = 0.2$). The error distributions used was taken from [48] which presents the reconstruction performance for contained cascades in AMANDA-II.

This histogram (using simulation data) would in a in the actual calibration situation be compared with a corresponding histogram for the *reconstructed* data. In the ideal situation these two histograms are expected to be samples from the same distribution. If the method for reconstructing cascade energies is not ideal this will affect the distribution. In particular, if the proportionality constant converting a cascade "size" into "energy" is not correct this will have the effect of shifting the mean value of the distribution.

10.3 Results

10.3.1 Calibration performance

As an example calibration scenario the prospect of identifying a generic defect in the reconstruction algorithm for E_{vis} will be examined – a misadjusted proportionality constant.

The expected distribution for $\log_{10}(E_{vis}/E_R)$ using an *ideal* reconstruction algorithm (see figure 10.2) was obtained for double-bang events in IceCube ($r_{min} = 100$ m) with uncertainties in both r and E_{vis} included. The mean ($m_0 = -0.31$)[*] and r.m.s. value ($\sigma_0 = 0.51$) was determined. These numbers may be used to test the standard reconstruction algorithm. For an algorithm that does not produce the proper proportionality between reconstructed and true values of E_{vis}, the distribution will suffer a shift (Δm) of its mean value.

[*] The mean m_0 is negative since the definition of E_R results in larger energy estimates than would an alternative *mean value* estimate. (A *mean value* estimate would have the drawback of resulting in a wider distribution.)

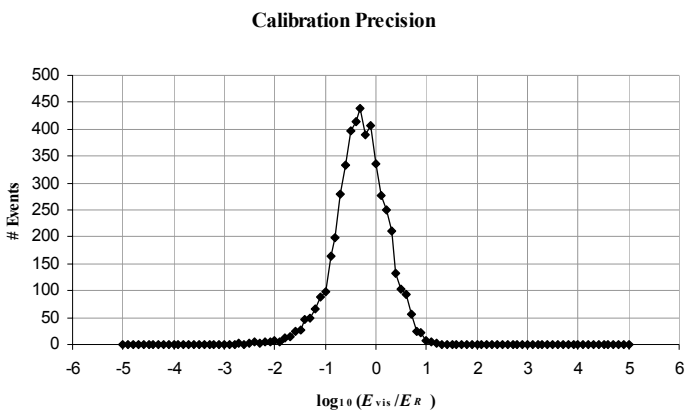

Figure 10.2. Distribution for $\log_{10}(E_{vis}/E_R)$ assuming correctly reconstructed double-bang events in IceCube (r_{min} = 100 m). E_{vis} is the measured cascade energy in the second cascade. E_R is the second-cascade energy as estimated from the measured tauon range. The "center-of gravity" is positioned at -0.31, and the r.m.s. value is 0.51.

After detecting N_{db} double bang events the mean value is estimated by $m = \langle \log_{10}(E_{vis}/E_R) \rangle$, and Δm is estimated by $(m\text{-}m_0)$. The minimum shift Δm_{min} that may be detected from this number of events depends on the aspired confidence level (CL). Given the approximation of regarding $\log_{10}(E_{vis}/E_R)$ to be an observation of a Gaussian distribution with standard deviation σ_0, a significant shift $\Delta m_{min} = |m\text{-}m_0|$ at 90% CL is

$$\Delta m_{min} = \frac{1.96 \cdot \sigma_0}{\sqrt{N_{db}}} \ . \qquad (10.9)$$

This corresponds to a systematic error in the reconstruction of a factor $\varepsilon^{\pm 1} = 10^{\pm \Delta m_{min}}$. Given a tau neutrino flux corresponding to the AMANDA-B10 limit presented in table 9.1 a one-year (live time) data sample will yield $\Delta m_{min} = 0.18$. In other words, if the standard reconstruction method under-estimates cascade energies by 30% or over-estimates by 50% this could be revealed by this method after a one-year exposure.

Chapter 11

Summary and outlook

The main topic for this thesis has been to try to investigate the prospects for energy calibration of cascade events in large neutrino telescopes, using cosmic tau neutrinos. In order to do so, three questions were formulated.

1) Are tau neutrinos of sufficient energy (~1 PeV) produced in nature?

Probably there does not exist any major production sites for "prompt" tau neutrinos. However, due to a phenomenon called neutrino mixing, which predicts that neutrinos will "oscillate" between neutrino "flavors" during propagation through space, it is not unlikely that all three flavors are equally abundant, as long as one only considers sources outside our solar system.

The expected flux contributions from such sources may be estimated in different ways. For *individual* source candidates theoretical models may be used to try to estimate their flux contributions. Examples on phenomena that has been modeled in this way are *Gamma Ray Bursters* (GRB) and *Active Galactic Nuclei* (AGN). For *classes* of source candidates one may e.g. use the observed flux of the high-energy *Cosmic Rays* (CR) to put limits on the neutrino flux. This approach has e.g. been used to derive an upper bound, which constrains the total neutrino flux from optically "thin" sources (first done by E. Waxman and J. Bahcall). The most straightforward approach, finally, is to try to constrain the neutrino flux through direct neutrino observations. One example is the upper limit derived from AMANDA-B10 (an earlier stage of AMANDA) data, taken during the austral winter 1997.

2) Will present or future neutrino telescopes be able to detect these tau neutrinos?

To answer that question one has to investigate the properties of such neutrino telescopes. In this thesis two detectors are described – AMANDA which has been deployed in the glacier ice near the geographical South Pole and IceCube which is a planned extension to AMANDA and will be deployed at the same location. These detectors use a detection technique of registering the emission of Čerenkov photons. This radiation is produced as electrically charged particles propagate through matter, e.g. as the electrically charged daughters from a neutrino-nucleon reaction propagate through the detector medium (ice).

The "signature" of these events depends on the flavor of the parent neutrino. Electron neutrinos result in single "cascade" events where the energy is deposited locally in the vicinity of the initial interaction vertex. Muon neutrinos will (in the case of charged current reactions) result in "track" events since the muons produced from these reactions are heavier then electrons and therefore more "penetrating". Tauons are heavier still, and one would expect tau neutrino reactions to produce tracks events as well. However, since the lifetime of a tauon is very small it will decay (producing a second cascade) before reaching very far, and thus retaining most of its initial energy. At relativistic energies time dilation becomes important, and the tauon range is proportional to its energy. The resulting signature will be two cascades separated by a tauon track. This is referred to as the "double-bang" signature.

Double bang events are at focus in this thesis, due to the useful linearity between the tauon energy and its range. By measuring the cascade separation it is possible to predict the energy of the second cascade (at the tauon decay vertex). This energy estimate may then be compared with the *measured* energy of the same cascade. Eventually – when enough statistics has been gathered – it is in principle possible to *calibrate* the method used for measuring cascade energies.

The principle is clear, and the next step is to try to estimate the annual number of double bang events. To do so one needs to know two things – the event rate in the detector medium and the detection probability. Both of these are energy dependent.

The event rate is expected to be described by a power law formula $\mathrm{d}N_{\mathrm{db}} / \mathrm{d}E_{\tau} \propto E_{\tau}^{-\alpha}$ where the spectral index $\alpha \approx 1.6$. Typical neutrino flux estimates were taken from the literature, but in the present study Monte Carlo simulations were used convert the given neutrino flux estimates to their corresponding double bang event rates.

The detection probability is expressed as an effective volume V_{eff}. It is defined as the volume, which multiplied with the double bang event rate per unit volume, yields the double bang detection rate (both cascades contained within the physical detector volume). An approximate expression for the effective volume was derived in this thesis. It has three free parameters. One of these – the minimum detectable cascade separation r_{min} – is assumed to be a known property of the detector. The other two – the detector "thickness" L and the "effective area" A_{eff} – was determined through Monte Carlo simulations. For AMANDA-II (the present – year 2003 – configuration of AMANDA) with $r_{\mathrm{min}} = 100$ m (an ad hoc value) the thickness and effective area were found to be $L \approx 260$ m and $A_{\mathrm{eff}} \approx 3.9 \cdot 10^4$ m^2 respectively. The effective volume rises sharply with increasing tauon energies, peaks at $E_{\tau} \approx 3$ PeV ($V_{\mathrm{eff}} \approx 1.2 \cdot 10^6$ m^3 – about 8% of the physical volume) and then falls off slowly with energy. For the proposed IceCube detector with a geometric volume approaching 1 km^3, $r_{\mathrm{min}} = 100$ m resulted in $L \approx 930$ m and $A_{\mathrm{eff}} \approx 9.0 \cdot 10^5$ m^2. IceCube was found both to be "sensitive" in a wider energy range compared with AMANDA-II. The peak value of the effective volume is positioned at $E_{\tau} \approx 5.5$ PeV ($V_{\mathrm{eff}} \approx 3.5 \cdot 10^8$ m^3 – about 39% of the physical volume).

Finally, by assuming an isotropic neutrino flux from "above" – the earth is essentially opaque to neutrinos at these energies and thus shields off the upward going neutrinos – enough information is at hand to estimate the detection rates for different proposed neutrino sources and neutrino flux upper limits. To exemplify, for AMANDA-II (with $r_{\min} = 100$ m) the AMANDA-B10 upper limit corresponds to 0.13 detected double bang events per year. IceCube (with $r_{\min} = 100$ m) this flux corresponds to 30 double bang events per year.

3) Can the double bang signature be used for calibration purposes?

In this thesis it is assumed that double bang events may be detected and recognized as such, and that the essential information may be "extracted" from data. The prospects for the proposed calibration method then relies on an essentially background free signal, a sufficiently high detection rate and a reasonably narrow distribution in the energy prediction based on the cascade separation.

The most serious background is assumed to come from charged current muon neutrino reactions where the muon travels approximately 100 m before loosing most of its energy in a single bremsstrahlung reaction. Rough calculations of the signal to noise ratio at the energy threshold for the detectors, ~ 2 PeV, yield a value of ~ 30 for AMANDA-II (with $r_{\min} = 100$ m) and ~ 80 for IceCube (with $r_{\min} = 100$ m). These values will improve if the minimum separation $r_{\min}$ is smaller than the assumed value.

The detection rates will clearly be too low for calibration purposes in the AMANDA-II detector. However, one must not forget that there is still at least one free parameter that might change this situation. To reach a possible detection rate of one double bang event per year (at the AMANDA-B10 upper limit) $r_{\min}$ would have to be close to ~ 60 m. For IceCube size detectors it is meaningful to investigate what it would take to be able to detect more pessimistic (realistic) flux estimates. E.g., to reach a detection rate of one double bang event per year at the Waxman-Bahcall limit in a 1 km^3 detector $r_{\min}$ would have to be close to ~ 25 m. This separation is similar to the expected (longitudinal) cascade lengths and is therefore probably very difficult to reach.

One may also argue that the detection rates will be larger if it turns out that the restriction of assuming fully contained events are too strict. It has been demonstrated that single cascades can be reconstructed even if they occur slightly outside the physical volume of the detector. However, since the uncertainties are larger in the reconstruction of position and energy of such cascade events, non-contained double bang events will probably not be suitable for calibration purposes.

The detection rates necessary for the proposed application – energy calibration of high energy cascades – depends on the possibility to determine the position and energy of the two cascades. It also depends on the intrinsic properties of the double bang events – how well the energy of the second cascade (at the tauon decay vertex) can be estimated from the cascade separation. For the precision and accuracy of determining the cascade positions, and for the precision in of the measurement of the cascade energy, values were assumed to be similar to what has been demonstrated for *single* cascades. This is clearly an optimistic assumption, but the important thing is not the quality of the measurement in it self so much as *knowing* what the quality is. The applicability of the calibration method will most likely be limited by the intrinsic properties. These properties have been determined through Monte Carlo simulations of neutrino-nucleon reactions.

To be able to examine the calibration method in quantitative terms an expression was derived for the "optimal" energy estimation as a function of cascade separation. A Monte Carlo simulation of double bang events, taking into account the described properties of the detection process, were used to produce "data" for the calibration. For each event the logarithm of the ratio between the "measured" energy (E_{vis}) of the second cascade and the *estimated* energy (E_R) was calculated. The distribution of these $\log_{10}(E_{\text{vis}}/E_R)$ values was found to be (roughly) Gaussian in shape. By observing that if the *measured* energy is over- or under estimated by a constant factor, this will result in a shift of the mean of this distribution. The standard deviation thus limits the resolution of the method. For IceCube (with $r_{\min} = 100\ \text{m}$) a one year exposure to a flux equal to the AMANDA-B10 upper limit a systematic under-estimation of the measured cascade energies by 30% (or more) will be detected at 90% CL. Similarly, if the measurement systematically over-estimates cascade energies by 50% or more, this will also be detected at 90% CL. This example concludes the study.

To go further it is necessary to evaluate the work already done. The principle of a calibration method has been demonstrated. Along the way, some phenomenological models have been developed to assist in studying the expected behavior of neutrino telescopes detecting double bang events. Also the intrinsic behavior of these events has been described in a "compact" manner. The next steps should include detailed detector simulations to produce as realistic "data" as possible. With these at hand one may start experimenting with different types of filter schemes and reconstruction methods. Then the possibilities for this method to become a practical method can be put to test. One crucial point is if there is a way to separate cascades appearing very closely in space. Perhaps the time information (photon hit times on the optical sensors) could be used in a very elaborate way.

One sub goal should be to try to identify these events accurately enough to be able to derive upper limits on the tau neutrino flux, thus contributing to the study of neutrino oscillation. If and when it is possible to detect double bang events at a sufficient rate and accurately measure their cascade energies and separation it is possible to invoke the proposed method for energy calibration.

Acknowledgements

In my work with AMANDA in general and in the preparation of this thesis I have received a lot of support and encouragement from many people around me. First of all I would like to thank Per-Olof Hulth at Stockholm University for his guidance and for sharing his deep insight into the experimental side of neutrino astrophysics. My first contact with the AMANDA-group however, was with Staffan Carius and Allan Hallgren. These inspiring teachers introduced me to the exciting world of scientific research as they guided me through my MSc project at Uppsala University. Staffan later became my mentor at Kalmar University, and he has continued to support and encourage me in my research even though I am no longer with the university. Even with his help finalizing this thesis would have been much more difficult without the support – e.g. by granting me very flexible working hours - from my bosses, Anders Werkström and Anders Rapp, during my two years at OKG AB.

The third "AMANDroid" to join up in Kalmar was Arvid Pohl. In him I have found a fantastic discussion partner and good friend, a true catalyst for extracting good ideas. Among the competent and dedicated staff in Kalmar I especially want to thank two of the computer "gurus", Claes Johansson and Stefan Petersson, who initially helped in getting the AMANDA work going by setting up the computer equipment and installing the necessary software. Also, Bo Rydberg must be acknowledged for his abilities in mechanical issues - constructing freezing containers and such - which is nothing less than outstanding. Thank you for your kind help.

I have made two trips to the AMANDA facility in Antarctica. At the *Amundsen Scott South Pole Station* I have met only capable and friendly people. In particular I have had the privilege to work closely with my good friend Julio Rodríguez Martino and with Ignacio Taboada. They shared my efforts regarding the diagnostic measurements on the AMANDA electronics. Julio and I worked together in November and December 1998, and Ignacio helped me when I returned one year later.

Regarding my work with simulations of particle reactions and detector responses I am grateful to Gunnar Ingelman and to Joakim Edsjö who introduced me to the `PYTHIA` code, and to Carlos Pérez de los Heros who showed me the ins and outs of `amasim`. I also want to thank Ariel Goobar and Lars Bergström for helping me getting a grasp of the *big* picture, e.g. by introducing me to some of the potential neutrino sources lurking "out there". Christian Walck has been a constant inspiration, especially in the field of mathematical statistics in which he is conversant both as a pragmatist and as a theoretician. Christian has also, together with Staffan Carius, Per-Olof Hulth and Klas Hultqvist, been my coach in finalizing this thesis.

Finally, I extend my warm thanks to my mother and father, Ann and Stig Lindahl, for allowing me to use their den whenever I needed to withdraw from every-day life to do my scientific scribbling, and to my wife and son, Pia and David Lindahl, for always welcoming me back!

Bibliography

[1] V.A. Balkanov et al., *Astroparticle Physics* **12** (1999) 75, astro-ph/9903341, "*Registration of Atmospheric Neutrinos with the BAIKAL Neutrino Telescope NT-96*"

[2] E. Aslanides et al., the ANTARES Collaboration. ANTARES Proposal, "*A Deep Sea Telescope for High Energy Neutrinos*", astro-ph/9907432

[3] E.G. Anassontzis et al., *Nucl. Phys. B (Proc. Suppl.)* **66** (1998) 247

[4] T. Montaruli for the NEMO Collaboration, M. Ambriola et al., 26th ICRC, HE 6.3.06, "*Capabilities of an Underwater Detector as a Neutrino Telescope and for the Neutrino Oscillation Search*", hep-ex/9905019

[5] E. Andres et al., the AMANDA Collaboration, *Astroparticle Physics* **13** (2000) 1, "*The AMANDA Neutrino Telescope: Principle of Operation and First Results*", astro-ph/9906203

[6] The IceCube Collaboration, "*IceCube: a Kilometer-Scale Neutrino Observatory, A Proposal to the National Science Foundation*", November 1999

[7] J.G. Learned, S. Pakvasa, *Astroparticle Physics* **3** (1995) 267, "*Detecting ν_τ Oscillations at PeV Energies"*, hep-ph/9405296

[8] D. N. Spergel et al., *Astrophysical Journal Supplement* **148** (2003) 175, "*First Year Wilkinson Microwave Anisotropy Probe (WMAP) Observations: Determination of Cosmological Parameters*", astro-ph/0302209

[9] S. Perlmutter et al, *Astrophys. J.* **517** (1999) 565-586, "*Measurements of Omega and Lambda from 42 High-Redshift Supernovae*", astro-ph/9812133

[10] M. Tegmark, M. Zaldarriaga, A. J. S. Hamilton, *Nuclear Physics B* (Proc. Suppl.) **91** (2001) 387-392, "*Weighing Neutrinos with Microwave Background and Galaxy Data*"

[11] The AMANDA Collaboration, *Phys. Rev. D* **66** (2002) 032006, "*Limits to the muon flux from WIMP annihilation in the center of the Earth with the AMANDA detector*", astro-ph/0202370

[12] L. Bergström, A. Goobar, *Cosmology and Particle Astrophysics*, Wiley, 1999

[13] A. Letessier-Selvon, *Nuclear Physics B* (Proc. Suppl.) **91** (2001) 473-479, "*Neutrinos and the Highest Energy Cosmic Rays*"

[14] H. Athar, *Astropart. Phys.* **14** (2000) 217-225, "*Neutrino Conversions in Cosmological Gamma-Ray Burst Fireballs*", hep-ph/0004191

[15] J. G. Learned, K. Mannheim, *Annu. Rev. Nucl. Part. Sci.* **50** (2000) 679-749, "*High-Energy Neutrino Astrophysics*"

[16] Y. A. Gallant, to appear in "*Relativistic Flows in Astrophysics*", eds. A.W. Guthmann et al, *Lecture Notes in Physics*, Springer Verlag, astro-ph/0201243

[17] R. Gandhi, *Nuclear Physics B* (Proc. Suppl.) **91** (2001) 453-461, "*Ultra-High Energy Neutrinos: A Review of Theoretical and Phenomenological Issues*", hep-ph/0011176

[18] K. Hagiwara *et al*., *Physical Review D* **66** (2002) 010001, "*The Review of Particle Physics*", `http://pdg.lbl.gov`

[19] The Super-Kamiokande Collaboration, (Talk presented at 8th International Workshop on Neutrino Telescopes, Venice, Italy, 23-26 Feb 1999) *Venice 1999, Neutrino telescopes,* **vol. 1** 183-201, "*Atmospheric Neutrinos at Super-Kamiokande*", hep-ex/9905016

[20] The SNO Collaboration, Submitted to *Physical Review Letters*, "*Measurement of the Total Active 8B Solar Neutrino Flux at the Sudbury Neutrino Observatory with Enhanced Neutral Current Sensitivity*", nucl-ex/0309004

[21] The KamLAND Collaboration, *Physical Review Letters* **90** (2003) 021802, "*First Results from KamLAND: Evidence for Reactor Antineutrino Disappearance*"

[22] R. Gandgi, C. Quigg, M. H. Reno, I. Sarcevic, *Phys. Rev. D* **58** (1998) 09009, "*Neutrino Interactions at Ultrahigh Energies*", hep-ph/9807264

[23] J. A. Castro Pena, G. Parente, E. Zas, *Physics Letters B* **500** (2001) 125-132, "*Measuring the BFKL Pomeron in Neutrino Telescopes*", hep-ph/0011043

[24] J. F. Beacom, P. Crotty, E. W. Kolb, *Physical Review D* **66** (2002) 021302, "*Enhanced signal of astrophysical tau neutrinos propagating through Earth*", astro-ph/0111482

[25] J. Alvarez-Muñiz, F. Halzen, D. W. Hooper, *Physical Review D* **62** (2000) 093015, "*High Energy Neutrinos from Gamma Ray Bursts: Event Rates in Neutrino Telescopes*", astro-ph/0006027

[26] F. W. Stecker, M. H. Salamon, *Space Sci. Rev.* **75** (1996) 341-355, "*High Energy Neutrinos from Quasars*", astro-ph/9501064

[27] E. Waxman, J. Bahcall, *Physical Review D* **59** (1999) 023002, "*High Energy Neutrinos from Astrophysical Sources: An Upper Bound*", hep-ph/9807282

[28] J. Ahrens et al., the AMANDA Collaboration, *Physical Review Letters* **90** (2003) 251101, "*Limits on Diffuse Fluxes of High Energy Extraterrestrial Neutrinos with the AMANDA-B10 Detector*", astro-ph/0303218

[29] J. D. Jackson, "*Classical Electrodynamics*" 2nd edition, Wiley (1975)

[30] A. Bouchta, PhD Thesis, Stockholm University, Department of Physics (1998), "*Muon Analysis with the AMANDA-B Four-String Detector*"

[31] C. Spiering, *Nuclear Physics B* (Proc. Suppl.) **91** (2001) 445-452, "*Future High Energy Neutrino Telescopes*", astro-ph/0012532

[32] E. Dalberg, PhD thesis, Stockholm University, Department of Physics (1999), "*A Search for Neutralino Dark Matter with the AMANDA-B10 Detector*"

[33] K. Woschnagg for the AMANDA collaboration, 26th ICRC, HE 4.1.15 (1999), "*Optical Properties of South Pole Ice from 140 to 2300 Meters*"

[34] P. Niessen, AMANDA – Internal Report 19981101 (1998), "*Simulated Bubbles and Their Effect on some Observables in AMANDA-B4*"

[35] J. Almlöf, F. Burmeister, Project Report, Uppsala University, Department of Radiation Sciences (1998), "*Minimisation of Air Bubbles in Ice*"

[36] P. Lindahl, AMANDA – Internal Report 20031103 (1998), "*Description of bubble formation during freezing of water in a cylindrical container*"

[37] P. Lindahl, MSc Thesis, Uppsala University, Department of Radiation Sciences (1997), "*Investigation of Timing Properties and Possibilities for Analog Pulse Detection for a Detector Channel of the Neutrino Telescope AMANDA*"

[38] P. Lindahl, AMANDA – Internal Report 19980501 (1998), "*Background trigger rates in AMANDA due to PMT dark noise*"

[39] S. Hundertmark, Proceedings of the Workshop on Simulation and Analysis Methods for Large Neutrino Telescopes DESY-Zeuthen, Germany, July 6-9, 1999, ed. C. Spiering, DESY-PROC-1999-01, ISSN 1435-8077, "*AMASIM neutrino detector simulation program*"

[40] P. Lindahl, AMANDA internal note presented in the collaboration meeting June 20-23 1999 in Uppsala, "*ELECTRA, an electronics simulation*"
[41] P. Lindahl, *AMANDA — Internal Report* 20031104 (2000), "*Diagnostic Measurements and Observations Regarding the Detector Channels in AMANDA B13*"
[42] A. Karle, P. Romenesko, *AMANDA — Internal Report* 19991001, "*Investigation into the observed gain instabilities of PMTs in the Ice using 1998 data*"
[43] A.R. Smith, R.J. McDonald, *AMANDA — Internal Report* 19990201, "*Radioactivities in AMANDA Optical Module #13-457*"
[44] C. Wiebusch, PhD thesis, Rheinishe Westfälishe Techniche Hochschule AAchen (1995), "*The Detection of Faint Light in Deep Underwater Neutrino Telescopes*"
[45] U. Amaldi, *Physica Scripta* **23** (1981) 409, "*Fluctuations in Calorimetry Measurements*"
[46] "*GEANT Detector Description and Simulation Tool*", CERN Program Library: `http://cernlib.web.cern.ch/cernlib/`
[47] I. Taboada, M. Kowalski for the AMANDA Collaboration, *Proceedings of* 27th ICRC (2001), HE 2.3 18:36, "*Search for Cascade-like events in the AMANDA-B10 detector*"
[48] M. Kowalski, I. Taboada, *AMANDA — Internal Report* 20020301, "*Cascade Reconstruction in AMANDA*"
[49] H. Lai et al. (CTEQ Collaboration), *Phys. Rev.* **D55** (1997) 1280
[50] D. Fargion, *Preprint INFN 1166/97*, astro-ph/9704205, "*The role of ντ ultrahigh energy astrophysics in km3 detectors*"
[51] T. Sjöstrand, *Computer Physics Commun*. **82** (1994) 74
[52] J. Klug, Diploma thesis, Uppsala University, Department of Radiation Sciences (1997), "*Enhancement of Up/Down Signal Ratio and Crosstalk Studies in AMANDA*"
[53] V. A. Kudryavtsev et al., "*Energy calibration of large underwater detectors using stopping muons*", hep-ex/0010056

List of Publications for Pär Lindahl

1997

1. **Author:** Pär Lindahl
   Title: *Investigation of Timing Properties and Possibilities for Analog Pulse Detection for a Detector Channel of the Neutrino Telescope AMANDA*
   Ref.: MSc thesis, Internal report ISV-10/1997, Uppsala University, December 1997

1998

2. **Author**: Pär Lindahl
   Title: *Background trigger rates in AMANDA due to PMT dark noise*
   Ref.: AMANDA – Internal Report 19980501 (1998)

3. **Author**: Pär Lindahl
   Title: *Description of bubble formation during freezing of water in a cylindrical container*
   Ref.: AMANDA – Internal Report 20031103 (1998)

2000

4. **Authors:** AMANDA Collaboration: E. Andrés et al
   Title: *The AMANDA Neutrino Telescope: Principle of Operation and First Results*
   Ref.: Astroparticle Physics **13** (2000) 1-20, March 2000

5. **Author**: Pär Lindahl
   Title: *Diagnostic Measurements and Observations Regarding the Detector Channels in AMANDA B13*
   Ref.: AMANDA — Internal Report 20031104 (2000)

2001

6. **Authors:** AMANDA Collaboration: E. Andrés et al
Title: *Observation of High-Energy Neutrinos Using Cerenkov Detectors Embedded Deep in Antarctic Ice*
Ref.: Nature **410** (2001) 441-443, 22 March 2001

2002

7. **Authors:** AMANDA Collaboration: J. Ahrens et al
Title: *Search for Supernova Neutrino-Bursts with the Amanda Detector*
Ref.: Astroparticle Physics **16** (2002) 345-359, February 2002

8. **Authors:** AMANDA Collaboration: J. Ahrens et al
Title: *Observation of High Energy Atmospheric Neutrinos with the Antarctic Muon and Neutrino Detector Array*
Ref.: Physical Review **D66** (2002) 012005, 1 July 2002

9. **Authors:** AMANDA Collaboration: J. Ahrens et al
Title: *Limits to the Muon Flux from WIMP Annihilation in the Center of the Earth with the AMANDA Detector*
Ref.: Physical Review **D66** (2002) 032006, 1 August 2002

2003

10. **Authors:** AMANDA Collaboration: J. Ahrens et al
Title: *Search for Neutrino-Induced Cascades with the AMANDA Detector*
Ref.: Physical Review **D67** (2003) 012003, 1 January 2003

11. **Authors:** AMANDA Collaboration: J. Ahrens et al
Title: *Search for Point Sources of High-Energy with AMANDA*
Ref.: Astrophysical Journal **583** (2003) 1040-1057, 23 January 2003

12. **Authors:** AMANDA Collaboration: J. Ahrens et al
Title: *Limits on Diffuse Fluxes of High Energy Extraterrestrial Neutrinos with the AMANDA-B10 Detector*
Ref.: Physical Review Letters **90** (2003) 251101, 24 June 2003

13. **Authors:** AMANDA Collaboration: J. Ahrens et al
Title: *Search for Extraterrestrial Point Sources of Neutrinos with AMANDA-II*
Ref.: e-print archive astro-ph/0309585, 22 September 2003